J. Fluid Mech. (1999), *vol.* 396, *pp.* 257–285. Printed in the United Kingdom

Intermittency and scaling of pressure at small scales in forced isotropic turbulence

By TOSHIYUKI GOTOH[1] AND ROBERT S. ROGALLO[2]

[1] Department of System Engineering, Nagoya Institute of Technology, Showa-ku, 466, Nagoya, Japan

[2] NASA-Ames Research Center, Moffett Field, CA 94035, USA

(Received 22 December 1997 and in revised form 30 April 1999)

The intermittency of pressure and pressure gradient in stationary isotropic turbulence at low to moderate Reynolds numbers is studied by direct numerical simulation (DNS) and theoretically. The energy spectra scale in Kolmogorov units as required by the universal-equilibrium hypothesis, but the pressure spectra do not. It is found that the variances of the pressure and pressure gradient are larger than those computed using the Gaussian approximation for the fourth-order moments of velocity, and that the variance of the pressure gradient, normalized by Kolmogorov units, increases roughly as $\mathscr{R}_\lambda^{1/2}$, where $\mathscr{R}_\lambda$ is the Taylor microscale Reynolds number. A theoretical explanation of the Reynolds number dependence is presented which assumes that the small-scale pressure field is driven by coherent small-scale vorticity–strain domains. The variance of the pressure gradient given by the model is the product of the variance of $u_{i,j}u_{j,i}$, the source term of the Poisson equation for pressure, and the square of an effective length of the small-scale coherent vorticity–strain structures. This length can be expressed in terms of the Taylor and Kolmogorov microscales, and the ratio between them gives the observed Reynolds number dependence. Formal asymptotic matching of the spectral scaling observed at small scales in the DNS with the classical scaling at large scales suggests that at high Reynolds numbers the pressure spectrum in these forced flows consists of three scaling ranges which are joined by two inertial ranges, the classical $k^{-7/3}$ range and a $k^{-5/3}$ range at smaller scale. It is not possible, within the classical Kolmogorov theory, to determine the length scale at which the inertial range transition occurs because information beyond the energy dissipation rate is required.

1. Introduction

The pressure field plays an important role in the turbulent motion of an incompressible fluid. In the Navier–Stokes equations the pressure gradient accelerates and deforms the fluid in a manner that prevents its dilatation. The pressure gradient is also of direct interest in practical problems such as particle dispersion, droplet growth, aerosol coagulation and turbulent sound generation by bubbles (Maxey 1987; Hill 1996).

The pressure is given formally by the solution of a Poisson equation with source term quadratic in the velocity gradient, which implies that moments of the pressure and pressure gradient are closely related to higher-order moments of velocity gradients. Heisenberg (1948) derived an expression for the variance of the pressure gradient by

assuming statistical independence of the Fourier amplitudes of the velocity field. The variance under this approximation is written as an integral of a quadratic function of the energy spectrum weighted by a geometrical factor.

Expressions for the two-point correlation of pressure and the variances of pressure and pressure gradient have been derived by Batchelor (1951) under the assumption that fourth-order and second-order moments of velocity are related as in a joint-normal distribution. He finds

$$\langle p(\boldsymbol{x}+\boldsymbol{r})p(\boldsymbol{x})\rangle_G = 2\bar{u}^4 \int_r^\infty \left(y - \frac{r^2}{y}\right)\left(\frac{\mathrm{d}f(y)}{\mathrm{d}y}\right)^2 \mathrm{d}y, \tag{1.1}$$

$$\langle (p(\boldsymbol{x}))^2\rangle_G = 2\bar{u}^4 \int_0^\infty y\left(\frac{\mathrm{d}f(y)}{\mathrm{d}y}\right)^2 \mathrm{d}y, \tag{1.2}$$

$$\langle (\nabla p(\boldsymbol{x}))^2\rangle_G = 12\bar{u}^4 \int_0^\infty \frac{1}{y}\left(\frac{\mathrm{d}f(y)}{\mathrm{d}y}\right)^2 \mathrm{d}y, \tag{1.3}$$

where p is the pressure–density ratio and will be referred to as simply 'the pressure' throughout the paper, $\bar{u}$ is the root mean square of one velocity component, $f(r)$ is the longitudinal velocity correlation function $\bar{u}^2 f(r) = \langle u_1(\boldsymbol{x}+r\boldsymbol{e}_1)u_1(\boldsymbol{x})\rangle$. Batchelor also shows that so far as fourth-order moments are concerned the assumption of statistical independence of Fourier amplitudes is equivalent to the joint normal approximation, and we shall refer to both as the Gaussian approximation. The subscript or superscript G, as in $\langle\cdot\rangle_G$ above, denotes an average using the Gaussian approximation for the velocity field. These classical formulae and their spectral equivalents have been used extensively to evaluate the pressure variances from more easily obtained velocity data (Batchelor 1951; Uberoi 1953; Schumann & Patterson 1978; George, Beuther & Arndt 1984). A characteristic length λ_p of the pressure gradient (Batchelor 1951) defined by

$$\left\langle \left(\frac{\partial p}{\partial x}\right)^2 \right\rangle = \frac{(\bar{u}^2)^2}{\lambda_p^2} \tag{1.4}$$

is an analogue of Taylor's microscale. When the universal equilibrium form for the velocity structure function

$$\langle (u_1(\boldsymbol{x}+r\boldsymbol{e}_1) - u_1(\boldsymbol{x}))^2\rangle = 2\bar{u}^2\,(1-f(r)) = (\bar{\epsilon}\nu)^{1/2}B(r/\eta) \tag{1.5}$$

is substituted into (1.1)–(1.3), we can compute the normalized variances of pressure

$$F_p = \frac{\langle p^2\rangle}{\left(\langle \boldsymbol{u}^2\rangle/2\right)^2} \tag{1.6}$$

and pressure gradient

$$F_{\nabla p} = \frac{\langle (\nabla p)^2\rangle}{\bar{\epsilon}^{3/2}\nu^{-1/2}} \tag{1.7}$$

respectively, where ν is the kinematic viscosity, $\bar{\epsilon}$ is the mean energy dissipation rate per unit mass, and $\eta = (\nu^3/\bar{\epsilon})^{1/4}$ is the Kolmogorov length. At high Reynolds numbers it is expected that $F_{\nabla p}$ is determined by scales within the universal equilibrium range and will therefore approach a constant. Batchelor (1951) estimated the asymptotic value $F_{\nabla p}^G = 3.9$ using (1.3) and the interpolated formula, $B(y) = y^2[1+(15C)^{-3/2}y^2]^{-2/3}/15$, with an absolute constant $C = 2$. Similar estimates were obtained by Chandrasekhar (1949) and Uberoi (1953). George *et al.* (1984) used the spectral equivalent of (1.1)

and an empirical energy spectrum for $E(k)$ and obtained

$$F_{\nabla p}^{G} = \left(3.7 - \frac{62.7}{\mathscr{R}_\lambda}\right), \tag{1.8}$$

which is close to Batchelor's result as $\mathscr{R}_\lambda \to \infty$. Since Taylor's microscale λ is related to $\bar{\epsilon}$ as (Tennekes & Lumley 1972)

$$\bar{\epsilon} = 15\nu\frac{\bar{u}^2}{\lambda^2}, \tag{1.9}$$

combining the definitions (1.7) and (1.9) with (1.4) we obtain

$$\frac{\lambda_p}{\lambda} = 5^{-1/2}15^{-1/4}\mathscr{R}_\lambda^{1/2}F_{\nabla p}^{-1/2}. \tag{1.10}$$

Within the universal equilibrium hypothesis this ratio is proportional to $\mathscr{R}_\lambda^{1/2}$ (Batchelor 1951). Equation (1.10) implies that as $\mathscr{R}_\lambda$ increases the scales contributing to the pressure-gradient variance become larger than those contributing to the dissipation.

The insensitivity of F_p to $\mathscr{R}_\lambda$ has been confirmed by DNS (Pumir 1994; Gotoh & Rogallo 1994; Cao, Chen & Doolen 1999; Vedula & Yeung 1999) and by experiment (Cadot, Douady & Couder 1995). On the other hand Yeung & Pope (1989) found the pressure-gradient variance, normalized by Kolmogorov scales, to vary as $\mathscr{R}_\lambda^{1/2}$ even though the velocity spectra scaled as required by universal equilibrium. That surprising and unexplained result was reproduced by Gotoh & Rogallo (1994) and Vedula & Yeung (1999). Hill & Wilczak (1995) obtained the structure function for pressure using an intermittency model for the fourth-order structure function of velocity gradients. Their results imply an $\mathscr{R}_\lambda^{3\mu/2}$ Reynolds number dependence for $F_{\nabla p}$ when the products of the two flatness factors of the longitudinal velocity derivative are assumed to be proportional to $\mathscr{R}_\lambda^{3\mu/2}$. With $\mu \approx 0.2$ (Sreenivasan & Kailasnath 1993; or $\mu = 0.25$, Praskovsky & Oncley 1994; $\mu = \frac{2}{9}$, She & Lévêque 1994), this dependence is weaker than the $\mathscr{R}_\lambda^{1/2}$ dependence found by DNS. Recent experimental studies also have shown that the variance of pressure gradient is larger than that obtained using the Gaussian approximation and that the difference between them becomes larger as $\mathscr{R}_\lambda$ increases (Hill & Thoroddsen 1997; Voth, Satyanarayan & Bodenschatz 1998).

The pressure spectrum, especially its scaling in the inertial range, has been previously examined. Kolmogorov scaling (Monin & Yaglom 1975) for the pressure spectrum gives

$$P(k) = \bar{\epsilon}^{4/3}k^{-7/3}\phi(k\eta), \tag{1.11}$$

where ϕ is a non-dimensional function. This spectrum is consistent with the prediction of the Gaussian approximation. George *et al.* (1984) measured the spectrum experimentally and found that it is close to $k^{-7/3}$, but certainty was prevented by the limited width of the inertial range and large measurement noise at high wavenumbers. Nelkin (1994) pointed out that the pressure difference $\delta_r p = p(\boldsymbol{x}+\boldsymbol{r}) - p(\boldsymbol{x})$ scales as the square of the velocity difference $\delta_r \boldsymbol{u} = \boldsymbol{u}(\boldsymbol{x}+\boldsymbol{r}) - \boldsymbol{u}(\boldsymbol{x})$, which implies the inertial-range exponent $-\frac{7}{3}$. Both George and Nelkin argue that the pressure spectrum follows classical Kolmogorov scaling rather than the mixed scaling suggested by its generalization for higher-order spectra by Van Atta & Wyngaard (1975). That generalization predicts $k^{-5/3}$ power spectra in an inertial range for all powers of the velocity and agrees well with measurements made in the atmospheric boundary layer.

Hill & Wilczak (1995) derived the spectrum $P(k) \propto k^{-7/3+2\mu/9}$, but the correction to the exponent is very small. Experimental data show that $\langle(\delta_r p)^2\rangle$ increases slower than $r^{4/3}$ for $r/\eta > 30$ at $\mathscr{R}_\lambda = 280$ (Hill & Boratav 1997).

High-resolution numerical simulations provide an effective means to obtain pressure statistics because the pressure field is exactly computed without deformation of the field, and without the introduction of any assumptions when the velocity field is well resolved. Pullin & Rogallo (1994) obtained pressure spectra by DNS and large-eddy simulation (LES) and examined their scaling based on Kolmogorov units, but could not reach a decisive conclusion about the inertial-range exponent. Their measurements within a simulated inertial range show that the spectrum has a level about three times that predicted by the Gaussian approximation. Gotoh & Rogallo (1994) compared pressure spectra from the same simulations with those produced by Gaussian velocity fields having the same energy spectra. It was found that the former are larger than the latter and that the difference between them increases with both Reynolds number and wavenumber. Yeung (1996) computed the two-particle Lagrangian acceleration correlation with small initial separation using DNS with a 512^3 mesh. He found that the contribution to the correlation from the viscous term is negligible compared to that from the pressure gradient up to $\mathscr{R}_\lambda = 200$ and beyond. He also observed fundamental differences between the longitudinal and transverse correlations. Cao *et al.* (1999) computed the pressure spectrum using DNS with 512^3 resolution and low-wavenumber forcing. They observed a $k^{-5/3}$ pressure spectrum, unlike the classical Kolmogorov inertial-range scaling and experimental observations. Their $\mathscr{R}_\lambda$ was limited to $\mathscr{R}_\lambda = 218$, and forcing was added at wavenumbers less than $k = 2.5$ to achieve a steady-state energy spectrum proportional to $k^{-5/3}$ within that range. Similar behaviour of the pressure spectrum has also been observed by Vedula & Yeung (1999) in a 512^3 DNS using a different forcing scheme. Surprisingly, there seems to be no consensus about the form of the pressure spectrum at present.

Since the source term of the Poisson equation for pressure is quadratic in the velocity gradient it is quite natural to expect non-Gaussian statistics for the pressure field even if the velocity gradient field were Gaussian. Recent studies of the small scales of turbulence have revealed that the PDFs for the vorticity and velocity gradients are themselves markedly different from Gaussian so we would expect even more deviation of the pressure PDF from the Gaussian. It is now widely accepted that the PDF for the pressure is negatively skewed and that its negative tail is exponential (Métais & Lesieur 1992; Holzer & Siggia 1993; Pumir 1994; Gotoh & Rogallo 1994; Cadot *et al.* 1995; Cao *et al.* 1999). The negative tail increases with $\mathscr{R}_\lambda$, while the positive tail remains close to Gaussian. Gotoh & Rogallo (1994) observed that the pressure-gradient PDF is strongly non-Gaussian but symmetric and its concavity increases with $\mathscr{R}_\lambda$. Regarding the large negative pressure fluctuations, Cadot *et al.* (1995) experimentally visualized low-pressure filaments in a turbulent shear flow using the micro-bubble technique, and found that the filaments correspond to regions of very low pressure, with deviations from the mean exceeding more than seven times the mean turbulent pressure intensity.

In this paper, we present measurements and analysis of pressure and pressure-gradient statistics in stationary isotropic turbulence obtained by forced DNS. Our purpose is, first to examine the Gaussian approximation for the fourth-order moments of the velocity and velocity gradient, which has been used in the past to evaluate the variances of pressure and pressure gradient, and to assess effects of the velocity and velocity gradient intermittency on the pressure and pressure gradient. Earlier work

(Batchelor 1951; Uberoi 1953; Chandrasekhar 1949; George *et al.* 1984) reported that the approximation was justified, but recent studies (Hill & Thoroddsen 1997) have shown that deviation from the Gaussian prediction exists and grows with $\mathscr{R}_\lambda$. The DNS data permit us to precisely examine the applicability of the Gaussian approximation, although $\mathscr{R}_\lambda$ is limited to rather low values. Our approach here is to measure the deviations of the pressure and pressure-gradient statistics from those predicted by Gaussian theory and to see how they change with $\mathscr{R}_\lambda$ and wavenumber. Secondly, in order to understand the underlying physics we present an argument that the $\mathscr{R}_\lambda$ dependence of $F_{\nabla p}$ is related to the spatial structure of the small-scale velocity field.

The paper is organized as follows. A review of the numerical simulation method and parameters are presented in § 2. In § 3, DNS results are presented for the variances of pressure and pressure gradient, the pressure spectrum, and the PDFs. Section 4 is devoted to an analysis of the pressure-gradient variance using a model field. Section 5 contains a summary and discussion.

2. Numerical simulation

The simulation algorithm used here, like those of Yeung & Pope (1989) and Cao *et al.* (1999), uses spectral spatial resolution, second-order time advance, and forcing at low wavenumbers to achieve accurate simulations of stationary turbulent flows. All of these simulations apply the forcing to a narrow band beginning at the lowest (fundamental) wavenumber in order to achieve the maximum Reynolds number possible. This results in bounded (strictly periodic) flows in which the energy resides in a very few Fourier modes at the largest available scales. This means first that the very small sample of energetic Fourier modes produce large fluctuations in statistical quantities with significant contributions from low wavenumbers, and second that energy backscatter into sub-harmonics is prevented, constraining (bounding) the flow.

A forced computation at moderate Reynolds numbers (but high enough to exhibit an inertial range in the energy spectrum) represents only the small scales of some high Reynolds number flow (the virtual flow). Within the classical Kolmogorov theory, it is not possible to relate the length and velocity scales (L, u) of the forced computation directly to those (L_0, u_0) of the virtual flow. We have only the relation $\bar{\epsilon} = u^3/L = u_0^3/L_0$, and the fact that the virtual and computed spectra match in their inertial ranges. When the Reynolds number is high enough, statistics in the virtual flow and the forced flow that depend only on scales within the universal equilibrium range should be the same. At low Reynolds number however such forced flows are very different from decaying flows. The asymptotic limit of large time for turbulence having small but finite Reynolds number at initial time is illustrative. For decaying turbulence the problem becomes linear at large time, the statistics depend explicitly on initial conditions, and the velocity spectrum rolls off exponentially like e^{-k^2} at high wavenumber. For forced turbulence the problem remains nonlinear (since equilibrium between transfer and dissipation is maintained), the statistics are independent of initial conditions, and the velocity spectrum would fall off much more slowly like e^{-k}. Because the results of all of the cited forced simulations deviate from classical Kolmogorov pressure scaling, the possibility of differences between bounded (periodic) and unbounded flows should be noted.

The turbulent flow fields used here (Jiménez *et al.* 1993) are all homogeneous and isotropic, and are held stationary by forcing a narrow band at low wavenumber

$\mathscr{R}_\lambda$	N^3	ν	E	$\bar{\epsilon}$	λ_p/λ	λ	$k_p\eta$	η	L_1
39	64^3	0.01	0.334	4.85×10^{-2}	0.735	0.830	0.696	0.0675	1.60
63	128^3	0.01	2.08	0.723	0.815	0.536	0.492	0.0342	1.36
96	256^3	0.02	53.8	106	0.879	0.318	0.371	0.0166	1.15
172	256^3	0.02	376	1600	0.963	0.217	0.253	0.0084	1.18

TABLE 1. Numerical parameters of simulations.

$|\boldsymbol{k}| < 2$ (Gotoh *et al.* 1993; Jiménez *et al.* 1993). The fields are arranged into four groups according to the Reynolds number $\mathscr{R}_\lambda$, with statistical quantities computed as averages over two fields at well separated times for $\mathscr{R}_\lambda = 172$ and over three fields for $\mathscr{R}_\lambda = 96, 63, 38$. The numerical grid sizes for the simulations ranged from $N = 256^3$ at $\mathscr{R}_\lambda = 172$ to $N = 64^3$ at $\mathscr{R}_\lambda = 38$, all of which satisfy the condition $K_{max}\eta \approx 2$. Due to computing constraints at Ames, the $\mathscr{R}_\lambda = 172$ fields were truncated to 256^3 ($K_{max}\eta \approx 1$) when our measurements were made. We have also used the large simulation of decaying isotropic turbulence of Wray (1997) to address the issues raised above. That simulation provides flow fields for $\mathscr{R}_\lambda \approx 65$ ($N = 512^3$) to $\mathscr{R}_\lambda \approx 32$ ($N = 256^3$) that have both a large sample of energetic modes and good resolution of the smallest scales. Throughout that Reynolds-number range, the measured energy spectra very accurately reproduce the experimental data of Comte-Bellot & Corrsin (1971).

Other numerical parameters are shown in table 1. The pressure field $p(\boldsymbol{k}, t)$ was computed from the velocity field using de-aliased spectral methods. The Gaussian velocity fields required for comparison were formed by randomizing DNS velocity fields. The required phase scrambling preserved both the energy and (zero) divergence of each three-dimensional Fourier velocity mode. The statistical quantities given in table 1 are total energy,

$$E = \frac{3}{2}\bar{u}^2 = \frac{\langle \boldsymbol{u}^2 \rangle}{2} = \int_0^\infty E(k)\,\mathrm{d}k, \tag{2.1}$$

average rate of energy dissipation per unit mass

$$\bar{\epsilon} = 2\nu \int_0^\infty k^2 E(k)\,\mathrm{d}k = \nu\Omega^2, \tag{2.2}$$

integral scale length

$$L_1 = \left(\frac{3\pi}{4}\int_0^\infty k^{-1}E(k)\,\mathrm{d}k\right)\Big/E, \tag{2.3}$$

Taylor's microscale

$$\lambda = \left(5E\Big/\int_0^\infty k^2 E(k)\,\mathrm{d}k\right)^{1/2}, \tag{2.4}$$

and microscale Reynolds number

$$\mathscr{R}_\lambda = \bar{u}\lambda/\nu. \tag{2.5}$$

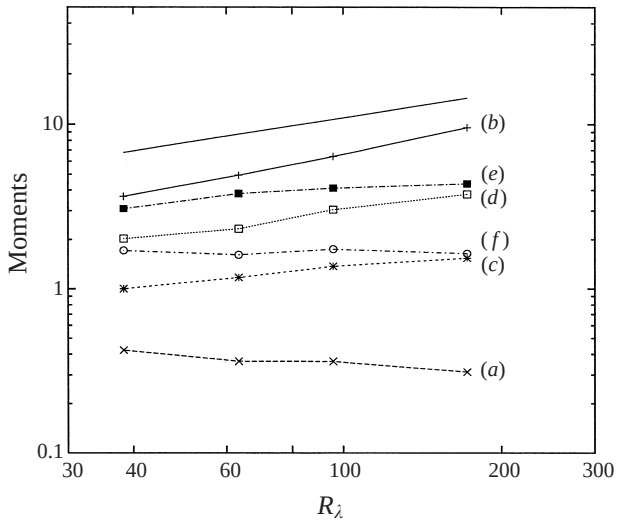

FIGURE 1. Variation with Reynolds number of various fourth-order moments of velocity. (*a*) F_p, (*b*) $F_{\nabla p}$, (*c*) F_ϵ, (*d*) F_ω, (*e*) $F_{\partial_1 u_1}$, (*f*) F_{u_1}. The slopes of curves (b, c, d) by least-square fit are 0.64, 0.29, 0.43, respectively. The solid line indicates $\mathscr{R}_\lambda^{1/2}$ behaviour.

3. Results

3.1. *One-point statistics*

The variation of F_p and $F_{\nabla p}$ with $\mathscr{R}_\lambda$ found in the DNS are shown in figure 1. Included there for comparison are other normalized fourth-order moments of velocity:

$$F_\epsilon = \frac{\langle \epsilon^2 \rangle}{\langle \epsilon \rangle^2} - 1, \quad F_\omega = \frac{\langle \omega^4 \rangle}{\langle \omega^2 \rangle^2} - 1, \quad F_{\partial_1 u_1} = \frac{\langle (\partial u_1/\partial x_1)^4 \rangle}{\langle (\partial u_1/\partial x_1)^2 \rangle^2} - 1, \quad F_{u_1} = \frac{\langle (u_1)^4 \rangle}{\langle (u_1)^2 \rangle^2} - 1. \tag{3.1}$$

The pressure variance F_p is relatively insensitive to $\mathscr{R}_\lambda$ in agreement with previous studies (Batchelor 1951; Uberoi 1953; Schumann & Patterson 1978; Pumir 1994). The pressure-gradient variance $F_{\nabla p}$, however, increases roughly as

$$F_{\nabla p} \approx A_1 \mathscr{R}_\lambda^{1/2} \tag{3.2}$$

for the range of Reynolds numbers studied, where A_1 is a constant of order unity. The rapid growth of $F_{\nabla p} \propto \mathscr{R}_\lambda^{1/2}$ was found earlier by Yeung & Pope (1989) from the variance of the total acceleration. On the other hand, the $\mathscr{R}_\lambda$ dependence of other moments is relatively slower than that of the pressure gradient, in agreement with the data of Kerr (1985).

Let us compare the pressure and its gradient from the DNS with those obtained from a Gaussian velocity field. As seen in figure 2 both $\langle p^2 \rangle$ and $\langle p^2 \rangle_G$ are rather insensitive to $\mathscr{R}_\lambda$ but $\langle p^2 \rangle_G$ (curve *b*) is about 20% lower than $\langle p^2 \rangle$ (curve *a*). The variance of the pressure gradient $\langle (\nabla p)^2 \rangle$ (curve *c*) is larger than $\langle (\nabla p)^2 \rangle_G$ (curve *d*) and grows more rapidly with $\mathscr{R}_\lambda$. The values of $F_{\nabla p}$ obtained from the simulation of decaying isotropic turbulence of Wray (1997) (curve *f*) are somewhat lower than those from the forced simulations (curve *c*) but higher than those resulting from the Gaussian approximation. At the highest computed Reynolds number they appear to

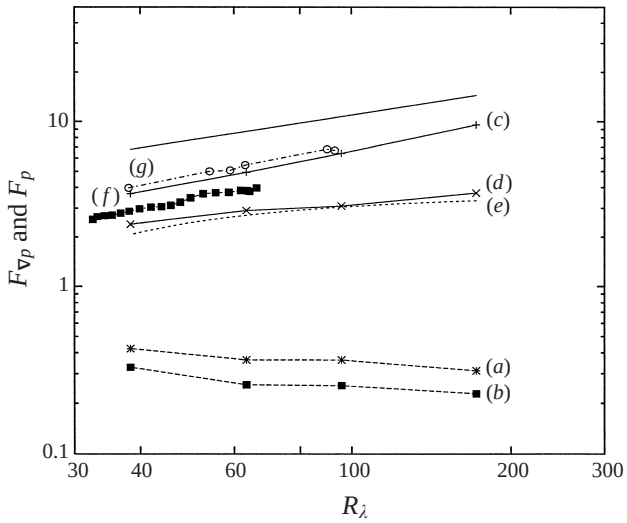

FIGURE 2. Comparison of DNS variances with those from the corresponding Gaussian velocity fields. (*a*) F_p (DNS), (*b*) F_p^G (Gaussian), (*c*) $F_{\nabla p}(DNS)$, (*d*) $F_{\nabla p}^G$ (present DNS-Gaussian), (*e*) $F_{\nabla p}^G$ (George *et al.* 1984, (1.8)), (*f*) $F_{\nabla p}$ (decaying run, Wray 1997), (*g*) $F_{\nabla p}$ (Yeung & Pope 1989). Batchelor's values for F_p and $F_{\nabla p}$ are 0.15 and 3.9, respectively. The solid line indicates $\mathscr{R}_\lambda^{1/2}$ behaviour.

approach the results of Batchelor (1951). Without knowledge of their behaviour at higher Reynolds number we cannot be certain that this is not fortuitous, but it seems quite likely that freely decaying flows will establish a universal equilibrium range at lower Reynolds number than forced flows that have their energy highly concentrated (and correlated) in a narrow scale range. This suggests that the deviation from Kolmogorov scaling in the forced simulations is an indication that the Reynolds number is not high enough, and the range of scales is not wide enough, for the small scales to become independent of the large driven scales.

The ratio of the characteristic length of the pressure gradient defined by (1.4) to Taylor's microscale is given by (1.10). Under the universal-equilibrium hypothesis this ratio is proportional to $\mathscr{R}_\lambda^{1/2}$ (Batchelor 1951). Our DNS measurements (figure 3) give (3.2) and the ratio of the length scales

$$\frac{\lambda_p}{\lambda} \approx A_2 \mathscr{R}_\lambda^{1/4}, \tag{3.3}$$

where A_2 is a constant of order unity. All of the data in figure 3 other than the DNS results (curves *a*, *e*, *f* and *g*) use the Gaussian approximation to relate pressure-gradient variance to second-order velocity correlations. They exhibit by construction length-scale ratios proportional to $\mathscr{R}_\lambda^{1/2}$ whenever the energy spectrum scales as required by universal equilibrium. The length-scale ratio from the DNS (curve *a*) grows approximately as $\mathscr{R}_\lambda^{1/4}$ for moderate Reynolds numbers and matches with the other data at low Reynolds numbers. It should be noted that the curve (*b*) from the randomized velocity field of the present DNS is higher than the DNS (curve *a*) and close to the other data resulting from the Gaussian approximation. This suggests that at large Reynolds numbers the Gaussian approximation considerably overestimates the scale separation between λ and λ_p.

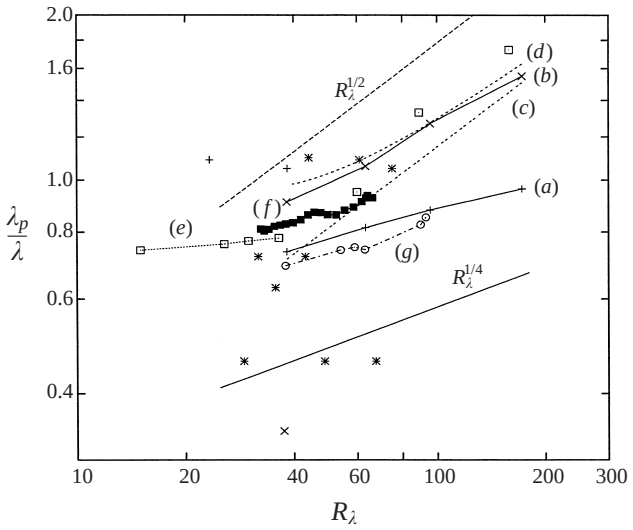

FIGURE 3. Variation of the ratio λ_p/λ with microscale Reynolds number: (*a*) present DNS, (*b*) present DNS-Gaussian, (*c*) Batchelor (1951), (*d*) George *et al.* (1984) (using (1.8), (1.10)), (*e*) Schumann & Patterson (1978), (*f*) decaying run, Wray (1997), (*g*) Yeung & Pope (1989); +, Collis (1948); ×, Simmons (1935); *, Uberoi & Corrsin (1952); □, Liepmann, Laufer & Liepmann (1951). The solid and dashed lines indicate $\mathscr{R}_\lambda^{1/4}$ and $\mathscr{R}_\lambda^{1/2}$ behaviour, respectively.

3.2. *Spectra*

The power spectrum of pressure (the pressure spectrum) $P(k)$ is related to the variances of pressure and its gradient by

$$\langle (p(\boldsymbol{x}))^2 \rangle = \int_0^\infty P(k)\,\mathrm{d}k, \tag{3.4}$$

$$\langle (\nabla p(\boldsymbol{x}))^2 \rangle = \int_0^\infty k^2 P(k)\,\mathrm{d}k. \tag{3.5}$$

The energy spectra for various $\mathscr{R}_\lambda$, compensated by $(k\eta)^{5/3}$ in figure 4, collapse well to a single curve as required by the universal-equilibrium hypothesis. The Reynolds numbers of the simulations are too low to expect a $k^{-5/3}$ inertial range behaviour however, and the form at low wavenumber is closer to $k^{-3/2}$. The pressure spectra, compensated by $(k\eta)^{5/3}\mathscr{R}_\lambda^{-1/2}$ in figure 5, collapse only at high wavenumber $k\eta > 0.3$, but tend to merge at lower wavenumber as the Reynolds number increases. The pressure spectra at low wavenumbers in figure 5 are closer to the $k^{-5/3}$ behaviour observed by Cao *et al.* (1999) and Vedula & Yeung (1999) than to the classic $k^{-7/3}$ inertial-range form. The variation of $F_{\nabla p}$ and $\bar{\epsilon}^{-3/4}\nu^{-7/4}P(k)$ with $\mathscr{R}_\lambda$, which includes large-scale information, indicates that the uniform equilibrium hypothesis is not valid for pressure statistics at the Reynolds number of these forced simulations.

It is useful to compare the scaling of the DNS pressure spectra in figure 5 with the scaling of the spectra in figure 6 obtained from the corresponding Gaussian velocity fields. In figure 6 the compensated pressure spectra are plotted with and without the $\mathscr{R}_\lambda^{-1/2}$ factor. Included in these figures are lines indicating the slope of $k^{-2/3}$. We conclude from figures 5 and 6 that the $\mathscr{R}_\lambda^{-1/2}$ factor is required for the scaling of the DNS pressure spectrum at high wavenumbers and that the situation for the

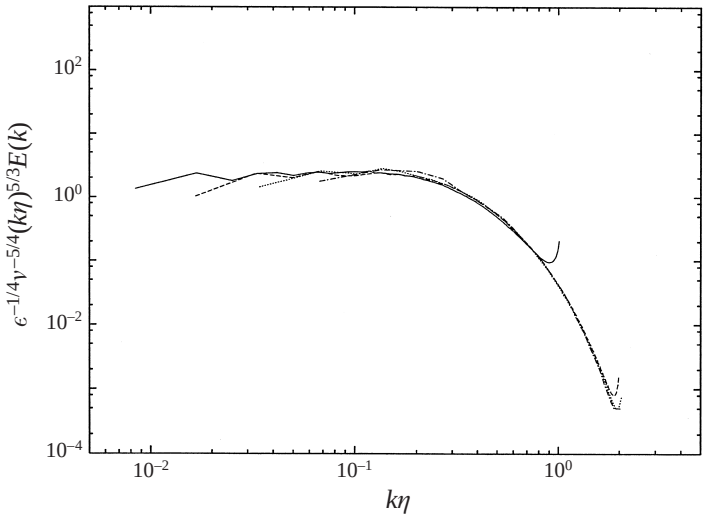

FIGURE 4. Compensated energy spectra in Kolmogorov units. ——— , $\mathscr{R}_\lambda = 172$; - - - - , $\mathscr{R}_\lambda = 96$; ····· , $\mathscr{R}_\lambda = 63$; —·— , $\mathscr{R}_\lambda = 38$.

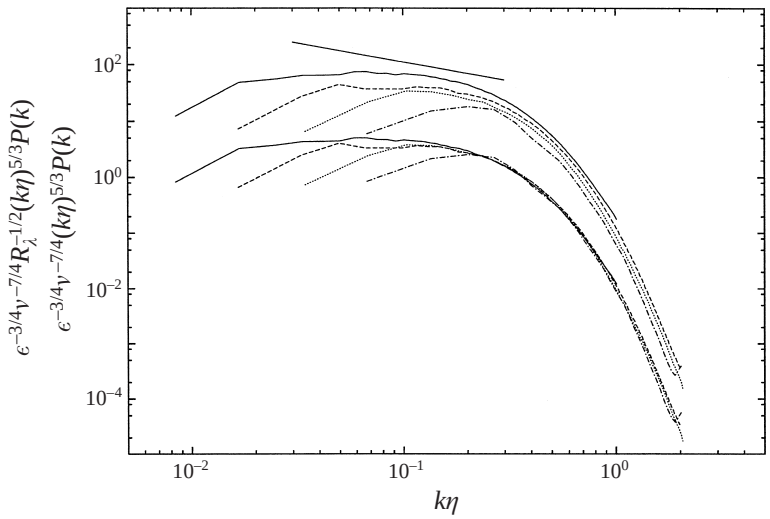

FIGURE 5. Reynolds-number scaling of the DNS pressure spectra. Upper curves: $\bar{\epsilon}^{-3/4}\nu^{-7/4}(k\eta)^{5/3}\ P(k)$. Lower curves: $\mathscr{R}_\lambda^{-1/2}\bar{\epsilon}^{-3/4}\nu^{-7/4}(k\eta)^{5/3}P(k)$. Line styles as in figure 4. The straight line indicates the slope of $k^{-2/3}$.

Gaussian spectrum $P_G(k)$ is quite the reverse. That is, scaling the Gaussian pressure spectra without the $\mathscr{R}_\lambda^{-1/2}$ factor collapses them well while scaling with the factor does not. The latter is expected since the Gaussian approximation equates the pressure spectrum to a function of the energy spectrum and the energy spectrum does follow Kolmogorov scaling. This indicates that the $\mathscr{R}_\lambda^{-1/2}$ factor is related to the structure of the velocity field at high wavenumber. The low-wavenumber tails of $k^{5/3}P_G(k)$ are similar to those of $k^{5/3}P(k)$ with or without the $\mathscr{R}_\lambda^{-1/2}$ factor. This suggests that the failure of the scaling at low wavenumbers is not directly due to intermittency effects.

Let us consider the scaling of the pressure spectrum. From figure 5 it appears that

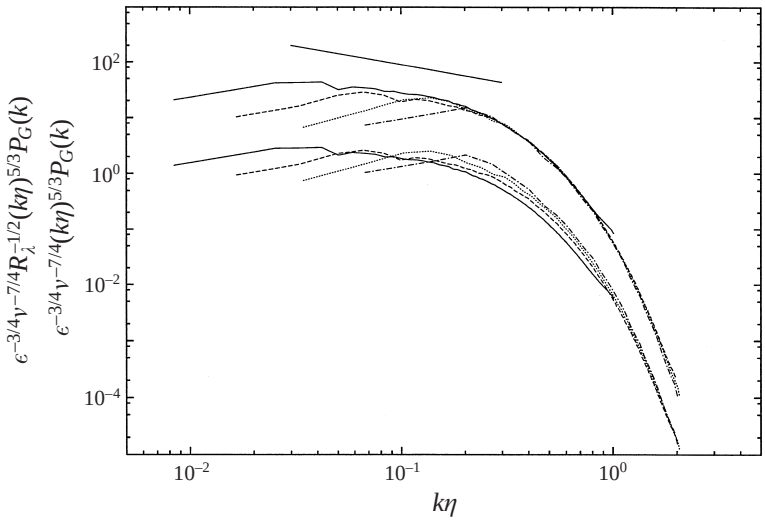

FIGURE 6. Reynolds-number scaling of pressure spectra in the Gaussian velocity fields. Upper curves: $\bar{\epsilon}^{-3/4}\nu^{-7/4}(k\eta)^{5/3}P_G(k)$. Lower curves: $\mathscr{R}_\lambda^{-1/2}\bar{\epsilon}^{-3/4}\nu^{-7/4}(k\eta)^{5/3}P_G(k)$. Line styles as in figure 4. The straight line indicates the slope of $k^{-2/3}$.

the pressure spectrum at high wavenumbers is

$$P(k) = \bar{\epsilon}^{3/4}\nu^{7/4}\mathscr{R}_\lambda^{1/2}\phi_1(k\eta), \tag{3.6}$$

where ϕ_1 is a non-dimensional function. If we assume that $P(k)$ at small wavenumber is scaled by the dissipation rate $\bar{\epsilon}$ and the internal length

$$L = u^3/\bar{\epsilon}, \tag{3.7}$$

which is of the same order as the integral scale L_1,

$$P(k) = \bar{\epsilon}^{4/3}L^{7/3}\phi_2(kL). \tag{3.8}$$

We note that the empirical relation $u^3 \propto \bar{\epsilon}L$ between the local velocity and length scales and the dissipation may be used to find equivalent forms of (3.8) within the large-scale and inertial ranges of the energy spectrum. Scaling by (3.8) collapses the spectra at low wavenumbers, but not as well as (3.6) does at high wavenumber (figure not shown). It is clear that at high Reynolds number (3.6) is not valid at the large scales since it would lead to a pressure variance of order $\mathscr{R}_\lambda^{1/2}$. The scaling forms (3.6) and (3.8) match asymptotically for large $\mathscr{R}_\lambda$ in an inertial range of the form

$$P(k) \propto \bar{\epsilon}^{4/3}L^{1/3}k^{-2}, \tag{3.9}$$

that is not consistent with either the classical $k^{-7/3}$ spectrum observed in experiments or the $k^{-5/3}$ spectrum observed in the simulations. We thus postulate an intermediate range of scales, based on the pressure microscale λ_p defined by (1.4) and the scaling

$$P(k) = \bar{\epsilon}^{4/3}\lambda_p^{7/3}\phi_2(k\lambda_p), \quad L^{-1} \ll k \ll \eta^{-1}. \tag{3.10}$$

This scaling matches (3.8) in a classical inertial range

$$P(k) \propto \bar{\epsilon}^{4/3}k^{-7/3}, \quad L^{-1} \ll k \ll \lambda_p^{-1}, \tag{3.11}$$

and matches (3.6) in the inertial range observed in the DNS

$$P(k) \propto \bar{\epsilon}^{4/3}\lambda_p^{2/3}k^{-5/3}, \quad \lambda_p^{-1} \ll k \ll \eta^{-1}. \tag{3.12}$$

At high Reynolds number the scales L, λ_p, and η become disparate as $L/\lambda_p = \lambda_p/\eta = \mathscr{R}_\lambda^{3/4}$.

This model spectrum is based only on the observed $\mathscr{R}_\lambda$ scaling of the Kolmogorov range within forced simulations at moderate Reynolds numbers, and the assumption that the scaling holds for sufficiently large $\mathscr{R}_\lambda$ to allow asymptotic matching. The matching itself does not prove the model, but merely shows that the model is consistent with both the classical Kolmogorov scaling and the observed computational results, and provides a link between the $\mathscr{R}_\lambda^{1/2}$ scaling factor and the $k^{-5/3}$ spectrum.

We do not expect the growing length of the $k^{-5/3}$ range, and resulting $\mathscr{R}_\lambda^{1/2}$ scaling factor, to continue indefinitely with increasing Reynolds number. Consider the flow of energy down the inertial range to smaller scale and lower Reynolds number. At any scale within an inertial range, the local Reynolds number, based on viscosity, local wavenumber, and global dissipation rate is

$$R_k = \nu^{-1}\bar{\epsilon}^{1/3}k^{-4/3} = (k\eta)^{-4/3}. \tag{3.13}$$

At high R_k the variety of structural instabilities (more generally, the variety of modes of structural evolution) is very large, consistent with the classical Kolmogorov cascade (local three-dimensional structural similarity). As the cascade proceeds, the variety of structural modes diminishes with decreasing R_k. Eventually there remains only the most robust (final) evolution mode, which is thought to be the roll-up of vortex sheets into strong vortex tubes. We thus postulate a critical Reynolds number R_* and scale $\lambda_p/\eta = R_*^{3/4}$ at which the cascade ceases to be scale similar, and where the $k^{-7/3}$ range ends. When $\mathscr{R}_\lambda$ within the simulations reaches R_* the spectrum at $k\eta > R_*^{-3/4}$, containing the $k^{-5/3}$ range, would become independent of $\mathscr{R}_\lambda$ and the normalized pressure-gradient variance would be bounded at order $R_*^{1/2}$. Further increase of $\mathscr{R}_\lambda$ would simply lengthen the $k^{-7/3}$ range at $k\eta < R_*^{-3/4}$ and the spectrum would follow classical Kolmogorov scaling throughout, with a significant but finite $(k\eta)^{-5/3}$ range at small scale. The proposed scaling is consistent with (3.11) and (3.12). When $k^2P(k)$ is integrated over $L^{-1} < k < \eta^{-1}$, the result is

$$F_{\nabla p} \propto \left(\frac{\lambda_p}{\eta}\right)^{2/3} + \left(\frac{\eta}{\lambda_p}\right)^{2/3} - 2\left(\frac{\eta}{L}\right)^{2/3}. \tag{3.14}$$

The full range of scales (L/η) is of order $\mathscr{R}_\lambda^{3/2}$. The span λ_p/η of the $k^{-5/3}$ range is of order $\mathscr{R}_\lambda^{3/4}$ when $\mathscr{R}_\lambda \leqslant R_*$ but is bounded at order $R_*^{3/4}$ when $\mathscr{R}_\lambda \geqslant R_*$. Thus asymptotic forms like (3.2) and (1.8) are recovered at low and high Reynolds numbers respectively.

The intermittency effects at small scales appear as an $\mathscr{R}_\lambda^{1/2}$ factor for the pressure-gradient variance and the scaling of the pressure spectrum, but it is not clear how the intermittency of the pressure field varies with wavenumber. One way to measure this variation is to compare the pressure spectrum $P(k)$ of the turbulence with the spectrum $P_G(k)$ computed from a Gaussian velocity field having the same energy spectrum (Chen *et al.* 1989).

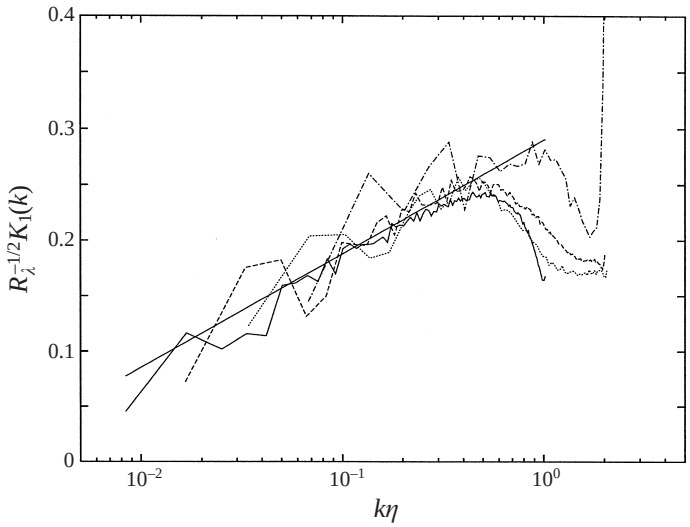

FIGURE 7. Variation of the (scaled) pressure-spectra ratio $\mathscr{R}_\lambda^{-1/2}K_1(k)$ with Reynolds number. The straight line is the fitted form $(2\mu/9)\log(k\eta) + 0.29$ with $\mu = 0.2$. Line styles as in figure 4.

We consider the spectrum ratio

$$K_1(k) = \frac{P(k)}{P_G(k)} \tag{3.15}$$

as a measure of the variation of pressure (and pressure gradient) intermittency across the spectrum. An $\mathscr{R}_\lambda^{1/2}$ dependence of $K_1(k)$ is again seen in the good collapse of $\mathscr{R}_\lambda^{-1/2}K_1(k)$ in figure 7 and the ratio can be written approximately as

$$K_1(k) \approx \mathscr{R}_\lambda^{1/2}\left[\frac{2\mu}{9}\log(k\eta) + 0.29\right], \quad k\eta \leqslant \tfrac{1}{2}. \tag{3.16}$$

The growth with wavenumber of the intermittency of second-order moments of the pressure field is very slow (it appears to be logarithmic, but the scale range is not sufficient to preclude a weak algebraic dependence). The constant $2\mu/9$ was obtained as follows. First, by using an appropriate theory, such as the refined scaling of Kolmogorov (1962) or the Log Poisson model of She & Lévêque (1994) for the fourth-order structure function $\langle(\delta_r u)^4\rangle$, we write $K_1(k) \propto \mathscr{R}_\lambda^{1/2}(k\eta)^{2\mu/9}$, and second, by expanding it to first order for small μ, we obtain the form (3.16). The constant 0.29 is estimated by inspection of figure 7. The fitted form agrees well with the four curves.

Since the power spectrum of pressure is formally related to a fourth-order moment of components of the velocity gradient tensor, it is illustrative to examine the power spectrum of the dissipation $\epsilon(\boldsymbol{x})$ which is formally related to a different fourth-order moment of components of the velocity gradient tensor. The power spectrum of the dissipation and its intermittency (ratio of turbulent to Gaussian spectra) are

$$\langle\epsilon^2(\boldsymbol{x})\rangle - \langle\epsilon\rangle^2 = \int_0^\infty E_\epsilon(k)\mathrm{d}k, \tag{3.17}$$

$$K_2(k) = \frac{E_\epsilon(k)}{E_{\epsilon,G}(k)}. \tag{3.18}$$

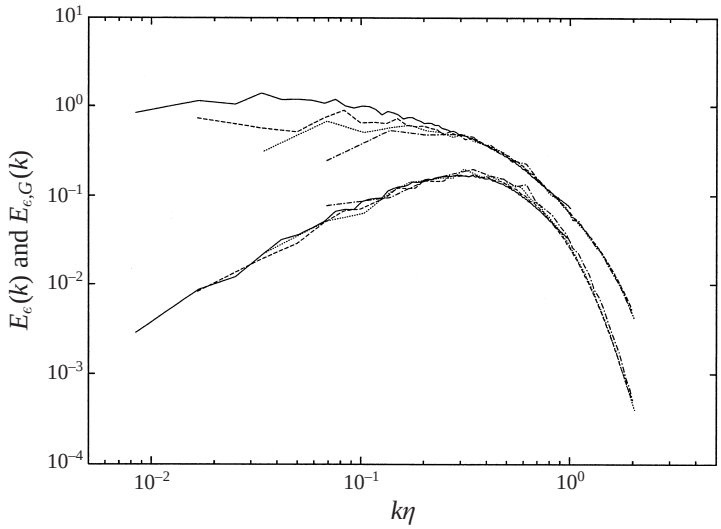

FIGURE 8. Comparison of dissipation spectra $E_\epsilon(k)$ and $E_{\epsilon,G}(k)$. Upper curves: $E_\epsilon(k)$. Lower curves: $E_{\epsilon,G}(k)$. Line styles as in figure 4.

Figure 8 shows a comparison of $E_\epsilon(k)$ and $E_{\epsilon,G}(k)$. It can be seen that $E_\epsilon(k)$ is nearly flat for $k_{min}\eta < k\eta < 0.3$ and decays slowly for $k\eta > 0.3$, while $E_{\epsilon,G}(k)$ has a peak at $k\eta \approx 0.3$. The spectra $E_\epsilon(k)$ collapse well for the high-wavenumber range of $k\eta > 0.3$ but not for lower wavenumbers, while $E_{\epsilon,G}(k)$ collapses for all wavenumbers. Similar results are also observed for power spectra of enstrophy ω^2 and can be understood with the aid of visualizations of the high vorticity and enstrophy domains within the DNS (She, Jackson & Orszag 1991; Jiménez *et al.* 1993; Cao *et al.* 1999; Tsinober 1998). Those domains are commonly observed to be localized in space (coherent structure) with one macroscale length and two smaller lengths of order of λ to η. The spectrum $E_\epsilon(k)$ then has support at low wavenumbers as well as at wavenumbers near $1/\lambda$ and $1/\eta$. On the other hand the dissipation in a Gaussian velocity field has no characteristic length scale other than η, so that its dissipation spectrum $E_{\epsilon,G}(k)$ has support only at wavenumbers of order $1/\eta$ and is narrower than that of $E_\epsilon(k)$. This point is to be discussed in the later sections.

The variation of the dissipation intermittency across the spectrum, indicated by the ratio $K_2(k)$ in figure 9, is a decreasing function of $k\eta$ when $k\eta < \frac{1}{2}$. For $k\eta > \frac{1}{2}$, $E_\epsilon(k)$ decreases slowly with wavenumber consistent with coherent structure such as vortex tubes within which there is well-organized dissipation associated with the rotational motion of fluid. The Gaussian spectrum $E_{\epsilon,G}(k)$, lacking such coherent structure, decreases rapidly with wavenumber so that $K_2(k)$ increases. It is interesting to note that the maximum of $K_1(k)$ and minimum of $K_2(k)$ both occur at $k\eta \approx \frac{1}{2}$, and that the diameter of intense vortex tubes is also of order η (Jiménez *et al.* 1993; Jiménez & Wray 1997). The strong variation of the dissipation intermittency across the spectrum is opposite to that of the pressure field (Chen *et al.* 1989).

3.3. *One-point PDF*

The one-point PDF for the pressure (figure 10) is skewed as reported by Pumir (1994) and Cadot *et al.* (1995). For negative pressure fluctuations its asymptotic form tends to be nearly exponential $Q(p) \propto \exp\left(-a|p/\sigma_p|^\gamma\right)$, where a is a non-dimensional

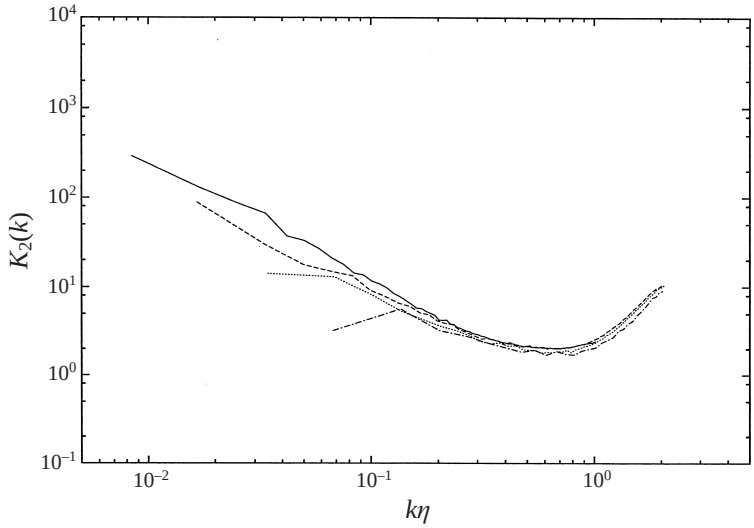

FIGURE 9. Variation of the dissipation-spectra ratio $K_2(k)$ with Reynolds number. Line styles as in figure 4.

constant, and $\sigma_p = (\langle p^2 \rangle - \langle p \rangle^2)^{1/2}$ is the pressure deviation. The tail of the PDF extends towards negative values with larger amplitude as $\mathscr{R}_\lambda$ increases. Although the tails of the PDFs do not extend far enough to define asymptotic values of a and γ, it is of interest to see what those values are. The constants a and γ were measured using a least-square fit within plots of $\ln(-\ln P(p))$ against $\ln p$ and are listed in table 2. The data for $\mathscr{R}_\lambda = 39, 65$ are not included due to the lack of asymptotic tails in the PDFs at those Reynolds numbers, and the values in table 2 are only rough estimates due to the small statistical sample of fields. The exponent γ is slightly smaller than one, consistent with low pressure in the core regions of intense vortex filaments, and is insensitive to $\mathscr{R}_\lambda$. For positive fluctuations the PDF is close to Gaussian and is insensitive to $\mathscr{R}_\lambda$. These results are consistent with the observations of Pumir (1994) and Cao *et al.* (1999). Furthermore the PDF $Q_G(p)$ of the pressure field computed from the corresponding Gaussian velocity field has a similar behaviour (figure 10) for the negative fluctuations as predicted by Holzer & Siggia (1993), but its negative tail is narrower than that of the actual PDF.

The PDFs for the pressure gradient $\partial p/\partial y$ (figure 11) are symmetric with tails that become wider as $\mathscr{R}_\lambda$ increases. They differ markedly from those computed from Gaussian velocity fields unlike the case of the pressure itself. The asymptotic tails of these PDFs appear to be much higher than exponential and the exponent δ, defined by $Q(p_{,i}) \propto \exp(-b\,|p_{,i}/\sigma_{p_{,i}}|^\delta)$, where $p_{,i} = \partial p/\partial x_i$ and b is a non-dimensional constant, is smaller than one and decreases slowly with $\mathscr{R}_\lambda$. On the other hand, δ for the Gaussian counterpart is about 1.13 for $\mathscr{R}_\lambda = 172$ which is close to unity as expected (Holzer & Siggia 1993). This suggests that the pressure-gradient field is very intermittent and is quite different from the pressure gradient in a Gaussian velocity field.

4. Theoretical analysis

We have seen in the previous section that in forced turbulence at low Reynolds number the normalized variance of the pressure gradient and the pressure spectrum at high wavenumber, i.e. the small scales of the pressure field, have a strong $\mathscr{R}_\lambda$

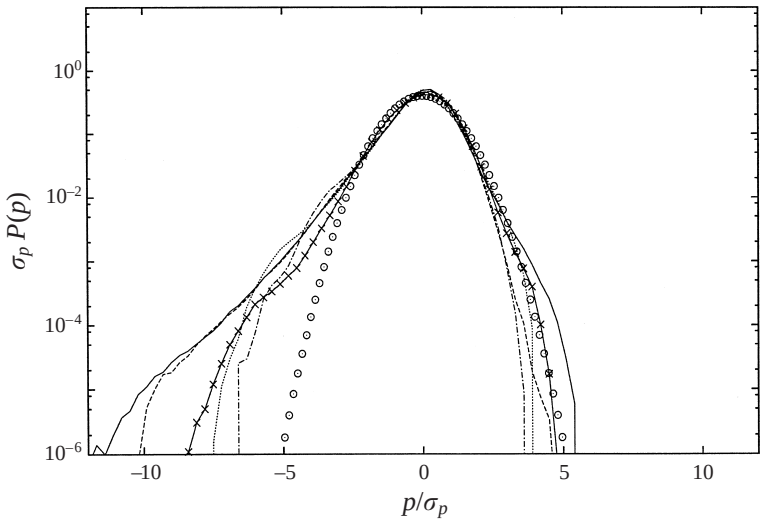

FIGURE 10. Variation of the PDF of pressure with Reynolds number. Line styles as in figure 4. — × — , Gaussian velocity field for $\mathscr{R}_\lambda = 172$; ○, Gaussian.

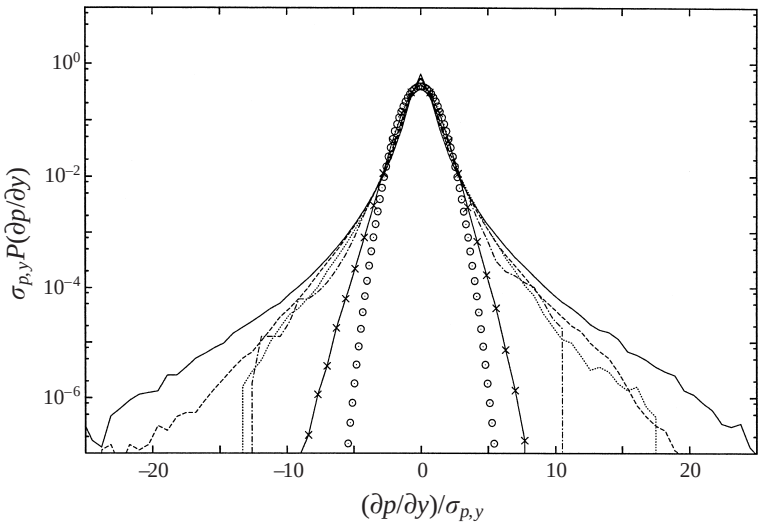

FIGURE 11. Variation of the PDF of $\partial p/\partial y$ with Reynolds number. Line styles as in figure 4. — × — , Gaussian velocity field for $\mathscr{R}_\lambda = 172$; ○, Gaussian.

dependence, while those for a Gaussian velocity field having the same kinetic energy spectrum do not. Yeung & Pope (1989) attempted to account for this $\mathscr{R}_\lambda$ dependence with a Kolmogorov (1962) correction, but the resulting $\mathscr{R}_\lambda$ dependence was much weaker than that observed in their simulations. The Kolmogorov (1962) correction is based on one-point statistics, and the structure of the velocity field does not enter explicitly. The differences between the statistics of turbulent and Gaussian fields is due to the presence of coherent structures in the turbulent vorticity and strain fields. It is commonly observed in DNS fields that the shape of those structures changes from three-dimensional blobs to two-dimensional sheets to one-dimensional tubes as

$\mathscr{R}_\lambda$	39	63	96	172
a	—	—	0.524	0.557
γ	—	—	0.861	0.840
b	0.630	0.869	0.960	1.131
δ	0.837	0.655	0.591	0.488

TABLE 2. Numerical constants of PDFs.

the threshold level for visualization is increased. On the other hand, by construction, no coherent structures exist in the Gaussian fields and it then seems quite natural to explain the $\mathscr{R}_\lambda$ dependence of the small-scale pressure statistics in terms of the relationship between the small scales of the pressure field and those small-scale coherent velocity-gradient structures.

In this section we determine the $\mathscr{R}_\lambda$ dependence of the pressure-gradient variance within a model turbulent flow. The fundamental idea is that the pressure gradient is mostly the result of the integral of a product of velocity derivatives over small coherent domains that have both macroscale and microscale dimensions, and that the ratio between those dimensions can give the observed Reynolds number dependence. The problem is how to construct a model that is consistent with various statistical constraints and the observations from DNS. We will illustrate the basic ideas here in a simplified version of the more detailed analysis that follows.

For an incompressible fluid, the pressure is determined by the Poisson equation

$$\nabla^2 p(\boldsymbol{x}) = S(\boldsymbol{x}), \tag{4.1}$$

$$S(\boldsymbol{x}) = -\frac{\partial u_j}{\partial x_i}\frac{\partial u_i}{\partial x_j} = \frac{\omega^2(\boldsymbol{x})}{2} - \sigma^2(\boldsymbol{x}), \quad \sigma^2 = \frac{1}{4}\left(\frac{\partial u_i}{\partial x_j} + \frac{\partial u_j}{\partial x_i}\right)^2, \tag{4.2}$$

where $\omega(\boldsymbol{x})$ is the amplitude of the vorticity and σ^2 is the square of the rate of strain tensor. The solution to (4.1) is given formally by

$$p(\boldsymbol{x}) = -\frac{1}{4\pi}\int \frac{S(\boldsymbol{y})}{|\boldsymbol{x}-\boldsymbol{y}|}\,\mathrm{d}\boldsymbol{y}. \tag{4.3}$$

In our discussion we shall omit contributions from boundaries as is appropriate for unbounded domains, and for our strictly periodic fields.

We wish to determine the dependence of the pressure-gradient variance on the structure of the pressure source S. Since the field is statistically homogeneous, we can write

$$\langle(\nabla p(\boldsymbol{x}))^2\rangle = \frac{1}{V}\int_V (\nabla p(\boldsymbol{x}))^2\,\mathrm{d}\boldsymbol{x}. \tag{4.4}$$

Assume that the support of $(\nabla p(\boldsymbol{x}))^2$ and S is composed of N similar but disjoint domains of volume V_s within the volume V. The position and orientation of the domains are not relevant since the integrand is a scalar without explicit spatial dependence. Then

$$\frac{1}{V}\int_V (\nabla p(\boldsymbol{x}))^2\,\mathrm{d}\boldsymbol{x} \approx \frac{NV_s}{V}\frac{1}{V_s}\int_{V_s} (\nabla p(\boldsymbol{x}))^2\,\mathrm{d}\boldsymbol{x}. \tag{4.5}$$

Using the relation $(\nabla p)^2 = \frac{1}{2}\nabla^2(p^2) - p\nabla^2 p$ we have

$$\frac{1}{V_s}\int_{V_s} (\nabla p(\boldsymbol{x}))^2 \,\mathrm{d}\boldsymbol{x} = \frac{-1}{V_s}\int_{V_s} p(\boldsymbol{x})S(\boldsymbol{x})\,\mathrm{d}\boldsymbol{x}$$

$$= \frac{1}{V_s}\int_{V_s}\frac{1}{4\pi}\int_{V_s}\frac{S(\boldsymbol{x})S(\boldsymbol{y})}{|\boldsymbol{x}-\boldsymbol{y}|}\,\mathrm{d}\boldsymbol{x}\,\mathrm{d}\boldsymbol{y}$$

$$= \frac{1}{4\pi}\int_{V_s}\frac{W(\boldsymbol{r})}{r}\,\mathrm{d}\boldsymbol{r}, \tag{4.6}$$

where

$$W(\boldsymbol{r}) = \frac{1}{V_s}\int_{V_s} S(\boldsymbol{y})S(\boldsymbol{y}+\boldsymbol{r})\,\mathrm{d}\boldsymbol{y}. \tag{4.7}$$

For an S domain of dimension l_1, l_2, l_3, having amplitude S and disparate scales $l_1 \gg l_2, l_3$, $W(\boldsymbol{r})$ is roughly estimated as

$$W(\boldsymbol{r}) \approx S^2\Theta(\boldsymbol{r}), \quad \Theta(\boldsymbol{r}) = \begin{cases} 1 & \text{for } \boldsymbol{r} \in V_s \\ 0 & \text{otherwise.} \end{cases} \tag{4.8}$$

Then (4.6) becomes

$$\frac{1}{V_s}\int_{V_s} (\nabla p(\boldsymbol{x}))^2\,\mathrm{d}\boldsymbol{x} \approx S^2\frac{l_1 l_2 l_3}{l_1} = S^2 l_2 l_3, \tag{4.9}$$

to leading order in $l_2/l_1 \ll 1$ (or $l_3/l_1 \ll 1$).

This is the crucial relation showing that the two-dimensional structure of S, as well as its amplitude, determines the pressure-gradient variance. Combining (4.4), (4.5), and (4.9)

$$\langle(\nabla p(\boldsymbol{x}))^2\rangle \approx \frac{NV_s}{V}S^2 l_2 l_3. \tag{4.10}$$

The extension to random S, $N(S)$, and $l_i(S)$ is found by introducing the PDF $Q(S) = V_s N(S)/V$ and integrating over S rather than $\boldsymbol{x}$:

$$\langle(\nabla p(\boldsymbol{x}))^2\rangle \approx \int_S S^2 l_2(S) l_3(S) Q(S)\,\mathrm{d}S. \tag{4.11}$$

Our more detailed analysis proceeds in three steps: first we introduce several exact statistical constraints, then we construct a model that is consistent with those constraints, and finally we compute the variance of the pressure gradient within the model.

4.1. *Statistical constraints*

The ensemble average of the pressure variance is

$$\langle(p(\boldsymbol{x}))^2\rangle = \frac{1}{16\pi^2}\iint\frac{\langle S(\boldsymbol{y})S(\boldsymbol{z})\rangle}{|\boldsymbol{x}-\boldsymbol{y}||\boldsymbol{x}-\boldsymbol{z}|}\,\mathrm{d}\boldsymbol{y}\,\mathrm{d}\boldsymbol{z}. \tag{4.12}$$

Since the turbulence is statistically homogeneous, the correlation function $\langle S(\boldsymbol{y})S(\boldsymbol{z})\rangle$ depends only on $\boldsymbol{r} = \boldsymbol{y} - \boldsymbol{z}$

$$\langle S(\boldsymbol{y})S(\boldsymbol{z})\rangle = W(\boldsymbol{r}), \tag{4.13}$$

(4.12) becomes

$$\langle(p(\boldsymbol{x}))^2\rangle = \frac{1}{16\pi^2}\iint\frac{W(\boldsymbol{r})}{|\boldsymbol{x}-\boldsymbol{y}||\boldsymbol{x}-\boldsymbol{y}-\boldsymbol{r}|}\,\mathrm{d}\boldsymbol{r}\,\mathrm{d}\boldsymbol{y}. \tag{4.14}$$

Following Kraichnan (1956), the $\boldsymbol{y}$ integration can be performed and we obtain the pressure variance

$$\langle p^2 \rangle = -\frac{1}{8\pi} \int W(\boldsymbol{r}) |\boldsymbol{r}| \, \mathrm{d}\boldsymbol{r}. \tag{4.15}$$

The variance of the pressure gradient is found in a similar manner to be

$$\langle (\nabla p)^2 \rangle = \frac{1}{4\pi} \int \frac{W(\boldsymbol{r})}{|\boldsymbol{r}|} \, \mathrm{d}\boldsymbol{r}. \tag{4.16}$$

We shall make use of two exact statistical constraints on the source term of the Poisson equation that follow from homogeneity, incompressibility, and the absence of boundary contributions:

$$\langle S \rangle = \frac{1}{V} \int S(\boldsymbol{x}) \, \mathrm{d}\boldsymbol{x} = \frac{-1}{V} \int \frac{\partial u_j}{\partial x_i} \frac{\partial u_i}{\partial x_j} \, \mathrm{d}\boldsymbol{x} = 0, \tag{4.17}$$

$$\int W(\boldsymbol{r}) \, \mathrm{d}\boldsymbol{r} = 0. \tag{4.18}$$

Since the left-hand sides of (4.15) and (4.16) are positive, combining (4.18) with the fact that (4.15) is weighted at large distance while (4.16) is weighted at short distance, we can conclude that

Fact 1. *The correlation $W(\boldsymbol{r})$ is positive at short distance and negative at large distance.*

When the turbulence is isotropic $W(\boldsymbol{r})$ is a function of r only and (4.18) becomes

$$\int_0^\infty W(r) r^2 \, \mathrm{d}r = 0. \tag{4.19}$$

Let us suppose that the source term $S(\boldsymbol{x})$ is given by the vorticity contribution alone. Then the correlation function for S becomes

$$\langle S(\boldsymbol{y} + \boldsymbol{r}) S(\boldsymbol{y}) \rangle = \tfrac{1}{4} \langle \omega^2(\boldsymbol{y} + \boldsymbol{r}) \omega^2(\boldsymbol{y}) \rangle. \tag{4.20}$$

When the separation r is large, $\omega^2(\boldsymbol{y} + \boldsymbol{r})$ and $\omega^2(\boldsymbol{y})$ are statistically independent so that

$$W(\boldsymbol{r}) \approx \tfrac{1}{4} \langle \omega^2(\boldsymbol{y} + \boldsymbol{r}) \rangle \langle \omega^2(\boldsymbol{y}) \rangle = O\left(\left(\frac{\bar{\epsilon}}{\nu} \right)^2 \right). \tag{4.21}$$

The right-hand side of (4.21) is constant for large r, which means that the integrals (4.15) and (4.16) diverge. The same divergence occurs for $S(\boldsymbol{x}) = -\sigma^2(\boldsymbol{x})$ and we conclude that

Fact 2. *It is essential for convergence of the integrals (4.15) and (4.16) that S takes both positive and negative values in space and that both vorticity and strain fields contribute equally to the integrals in the sense of (4.18) or (4.19).*

The model turbulent flow must then contain both vorticity and strain fields and satisfy the exact statistical constraints (4.17) to (4.19).

4.2. *A model of homogeneous isotropic turbulent flow*

We wish to construct a coherent-structure model for the source term of the pressure equation that produces the observed Reynolds number dependence. But what is a

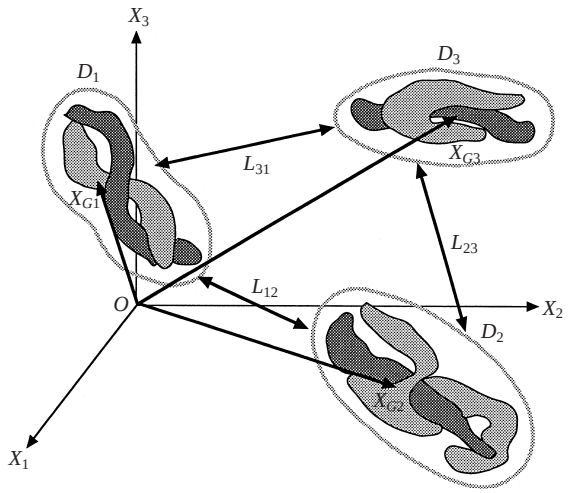

FIGURE 12. Schematic of a model pressure source field consisting of coherent domains. Each domain contains regions with positive S (dark shaded region) and negative S (light shaded region). The domains are separated by a distance of the order of the integral scale L_{ij}.

coherent structure? A coherent structure, in the context of this paper, is defined as follows.

Definition. *Coherent structure is a spatial configuration of domains, in each of which a physical quantity with values above a given threshold has strong spatial correlation with at least one macroscale length.*

An assembly of vortex tubes is a well-known example. It seems natural from the discussion following (4.21) and from (4.18) or (4.19) to expect that vorticity- and strain-dominated domains are located adjacent in space. One example of this configuration can be seen in figure 12 of Cao *et al.* (1999). Close inspection of the figure reveals that a domain of high vorticity is, roughly speaking, accompanied by a nearby domain of high strain. Another example is Burgers' vortex in which strong vorticity is concentrated near the axis while the maximum strain is located in the region surrounding the vortex core. Based on these observations we propose a coherent-structure model for the pressure-source field as follows (see also figure 12).

A model source field. *A turbulent flow with coherent structure of S consists of an infinite number of disjoint S-domains distributed uniformly and isotropically with macroscale separation, each of which contains a region of high vorticity and an adjacent region of high strain.*

We denote the union of adjacent vorticity–strain regions as D_α, in which S takes positive and negative values with high amplitudes. For simplicity we assume that this domain is a randomly oriented ellipsoid with dimensions $\tilde{l}_1 \geqslant \tilde{l}_2 \geqslant \tilde{l}_3$. The intensity and lengths of each domain D_α vary randomly. Now we put forth the basic assumption.

Assumption A. *The pressure gradient is determined only by contributions from the*

coherent domains D_α with large S amplitude, and contributions from regions outside the domains can be neglected.

This is a reflection of the fact that $\langle(\nabla p)^2\rangle$ is dominated by the contributions of the correlation function for S at short separation (see (4.16)).

4.3. *Computation of the variance of pressure gradient*

Computation of the pressure-gradient variance from the model source field consists of three steps. First we start from (4.3) for one realization of the model field and show that the square of the pressure gradient is given approximately by an integral of the square of the source term over the average coherent domain $\bar{D}$. In the second step, a formula for the variance of the pressure gradient is derived as the product of the variance of the source term and the square of a length characterizing the average volume of a coherent domain. In the third step, we estimate this length using the PDF for the velocity gradient and results of visualization of the small scales obtained by recent DNS. This gives the Reynolds number dependence of the normalized variance of the pressure gradient.

Step 1.

For one realization the square of the pressure gradient at a point $\boldsymbol{x}$ in a laboratory frame is

$$(\nabla p(\boldsymbol{x}))^2 = \frac{1}{16\pi^2}\iint_{\mathscr{D}} S(\boldsymbol{y})S(\boldsymbol{z})\nabla_{\boldsymbol{y}}\nabla_{\boldsymbol{z}}\left(\frac{1}{|\boldsymbol{x}-\boldsymbol{y}||\boldsymbol{x}-\boldsymbol{z}|}\right)\mathrm{d}\boldsymbol{y}\,\mathrm{d}\boldsymbol{z}, \tag{4.22}$$

where the integration is taken over $\mathscr{D}$, the union of all D_α, $\mathscr{D} = \bigcup_{\alpha=1}^{\infty} D_\alpha$. For this field, the pressure gradient fluctuates randomly with $\boldsymbol{x}$. We take the volume average of (4.22) as

$$\begin{aligned}\overline{(\nabla p)^2}^V &\equiv \frac{1}{V}\int_V (\nabla p(\boldsymbol{x}))^2\,\mathrm{d}\boldsymbol{x}\\ &= \frac{1}{16\pi^2 V}\iint_{\mathscr{D}} S(\boldsymbol{y})S(\boldsymbol{z})\ \nabla_{\boldsymbol{y}}\nabla_{\boldsymbol{z}}\left(\int_V \frac{1}{|\boldsymbol{x}-\boldsymbol{y}||\boldsymbol{x}-\boldsymbol{z}|}\,\mathrm{d}\boldsymbol{x}\right)\mathrm{d}\boldsymbol{y}\,\mathrm{d}\boldsymbol{z},\end{aligned} \tag{4.23}$$

where V is a large volume of the model turbulence field. Using the same technique that lead to (4.16), we perform the $\boldsymbol{x}$ integration and obtain

$$\overline{(\nabla p)^2}^V = \frac{1}{4\pi V}\iint_{\mathscr{D}} \frac{S(\boldsymbol{y})S(\boldsymbol{y}+\boldsymbol{r})}{|\boldsymbol{r}|}\,\mathrm{d}\boldsymbol{y}\,\mathrm{d}\boldsymbol{r}. \tag{4.24}$$

Due to statistical homogeneity, the left-hand side of (4.24) is equal to the ensemble average $\langle(\nabla p(\boldsymbol{x}))^2\rangle$ and the $\boldsymbol{y}$ integral of the right-hand side of (4.24) is equal to the ensemble average

$$\frac{1}{V}\int_{\mathscr{D}} S(\boldsymbol{y})S(\boldsymbol{y}+\boldsymbol{r})\,\mathrm{d}\boldsymbol{y} = \langle S(\boldsymbol{y})S(\boldsymbol{y}+\boldsymbol{r})|\mathscr{D}\rangle, \tag{4.25}$$

where $\langle\cdot|\mathscr{D}\rangle$ denotes the ensemble average over coherent domains $\mathscr{D}$. Then we have

$$\langle(\nabla p)^2\rangle = \frac{1}{4\pi}\int \frac{\langle S(\boldsymbol{y})S(\boldsymbol{y}+\boldsymbol{r})|\mathscr{D}\rangle}{|\boldsymbol{r}|}\,\mathrm{d}\boldsymbol{r}, \tag{4.26}$$

which is very similar to (4.16). The difference is that the average is now taken over the ensemble of coherent domains.

Non-zero contributions to the left-hand side of (4.25) can occur only when $\boldsymbol{y}$ is in D_α and $\boldsymbol{y}+\boldsymbol{r}$ in D_β. When $\alpha=\beta$, the values of $S(\boldsymbol{y})$ and $S(\boldsymbol{y}+\boldsymbol{r})$ are of the same order of magnitude due to the strong spatial correlation (coherency), that is

$$S(\boldsymbol{y})S(\boldsymbol{y}+\boldsymbol{r}) \approx S_0^2(\boldsymbol{X}_{G\alpha}) \quad \text{for } \alpha=\beta, \tag{4.27}$$

where $S_0^2(\boldsymbol{X}_{G\alpha})$ is the square of the amplitude S at the centre $\boldsymbol{X}_{G\alpha}$ of the domain D_α. On the other hand, when $\alpha \neq \beta$,

$$S(\boldsymbol{y})S(\boldsymbol{y}+\boldsymbol{r}) \approx S_0(\boldsymbol{X}_{G\alpha})S_0(\boldsymbol{X}_{G\beta}) \quad \text{for} \alpha \neq \beta. \tag{4.28}$$

Combining (4.27) and (4.28) with (4.25) yields

$$\begin{aligned}\langle S(\boldsymbol{y})S(\boldsymbol{y}+\boldsymbol{r})|\mathscr{D}\rangle &= \langle S(\boldsymbol{y})S(\boldsymbol{y}+\boldsymbol{r})|\mathscr{D};\boldsymbol{y},\boldsymbol{y}+\boldsymbol{r},\ \text{same domain}\rangle \\ &\quad +\langle S(\boldsymbol{y})S(\boldsymbol{y}+\boldsymbol{r})|\mathscr{D};\boldsymbol{y},\boldsymbol{y}+\boldsymbol{r},\ \text{different domain}\rangle \\ &\approx \langle S(\boldsymbol{y})S(\boldsymbol{y}+\boldsymbol{r})|\mathscr{D}\rangle_d + \langle S(\boldsymbol{y})|\mathscr{D}\rangle^2 \\ &\approx \langle S(\boldsymbol{y})S(\boldsymbol{y}+\boldsymbol{r})|\mathscr{D}\rangle_d, \end{aligned} \tag{4.29}$$

where the subscript d of $\langle S(\boldsymbol{y})S(\boldsymbol{y}+\boldsymbol{r})|\mathscr{D}\rangle_d$ denotes diagonal in α for suffix of D_α. We have used fact that macroscale separation between D_α and D_β ($\alpha \neq \beta$) ensures their statistical independence, and that the average $\langle S(\boldsymbol{y})|\mathscr{D}\rangle$ vanishes because of (4.17) and by model construction using regions of positive and negative S. Since the field is statistically homogeneous, the right-hand side of the last line of (4.29) is independent of $\boldsymbol{y}$. Equations (4.26) and (4.29) state that the variance of the pressure gradient is determined by the weighted integral of the source term over the average volume of one coherent domain, that is, over $\overline{D}$.

Step 2.

In order to obtain an approximate form for $\langle S(\boldsymbol{y})S(\boldsymbol{y}+\boldsymbol{r})|\mathscr{D}\rangle_d$, we define more precisely the set of coherent structures D_α. Let $\boldsymbol{X}_{G\alpha}$ be the centre of the αth domain of the coherent structure. The shape of one domain D_α is approximately an ellipsoid with three lengths $\tilde{l}_1 \geqslant \tilde{l}_2 \geqslant \tilde{l}_3$. We attach to the domain unit vectors $\boldsymbol{n}$ parallel to the $\tilde{l}_1$-direction and $\boldsymbol{b}$ parallel to the $\tilde{l}_2$-direction. A local coordinate system is introduced with its origin at $\boldsymbol{X}_{G\alpha}$, x_1-axis parallel to $\boldsymbol{n}$, x_2-axis parallel to $\boldsymbol{b}$, and x_3-axis parallel to $\boldsymbol{n}\times\boldsymbol{b}$. If we introduce a non-dimensional function w and amplitude $S_0 = S(\boldsymbol{x}=0)$, $S(\boldsymbol{x})$ can be written as

$$S(x_1,x_2,x_3) = S_0 w(x_1/\tilde{l}_1, x_2/\tilde{l}_2, x_3/\tilde{l}_3), \tag{4.30}$$

where the function w is assumed to depend on the shape of D_α only through $\tilde{l}_i(S_0)(i=1,2,3)$. The amplitude of w is assumed to be of order unity within the domain and to rapidly decay to zero outside it.

Consider a sub-ensemble of domains D_α with given values of $\boldsymbol{n},\boldsymbol{b}$ and S_0. Using (4.30) and averaging the product over the above sub-ensemble, we obtain

$$\langle S(\boldsymbol{y})S(\boldsymbol{y}+\boldsymbol{r})|\boldsymbol{n},\boldsymbol{b},S_0;\mathscr{D}\rangle_d = S_0^2\langle w(\boldsymbol{y})w(\boldsymbol{y}+\boldsymbol{r})|\boldsymbol{n},\boldsymbol{b},S_0;\mathscr{D}\rangle_d\ . \tag{4.31}$$

Since both $\boldsymbol{y}$ and $\boldsymbol{y}+\boldsymbol{r}$ are in the same domain, we expect from the definition of the coherent structure that $w(\boldsymbol{y})w(\boldsymbol{y}+\boldsymbol{r})$ is of order unity for $|r_i|/\tilde{l}_i \lesssim 1$ and decays rapidly to zero for $|r_i|/\tilde{l}_i \gtrsim 1$. Therefore we may write

$$\langle w(\boldsymbol{y})w(\boldsymbol{y}+\boldsymbol{r})|\boldsymbol{n},\boldsymbol{b},S_0;\mathscr{D}\rangle_d = \Theta(r_1/l_1, r_2/l_2, r_3/l_3), \tag{4.32}$$

where $l_i = l_i(S_0)$ denotes the average of $\tilde{l}_i$ over the sub-ensemble, i.e.

$$l_i(S_0) \equiv \langle \tilde{l}_i \mid S_0; \mathscr{D} \rangle. \tag{4.33}$$

The function Θ measures the coherency of S at two points separated by $\boldsymbol{r}$ within the average domain with dimensions $l_1 \times l_2 \times l_3$. We denote this conditionally averaged volume simply as $\bar{D}$. Note that the right-hand side of (4.32) does not depend on $\boldsymbol{y}, \boldsymbol{n}$ or $\boldsymbol{b}$ by homogeneity and isotropy, and by construction.

Combining (4.29), (4.31) and (4.32) with (4.26) yields

$$\begin{aligned}
\langle (\nabla p)^2 \rangle &\approx \frac{1}{4\pi} \int \langle S(\boldsymbol{y}) S(\boldsymbol{y}+\boldsymbol{r}) | \mathscr{D} \rangle_d \ |\boldsymbol{r}|^{-1} \, \mathrm{d}\boldsymbol{r} \\
&\approx \frac{1}{4\pi} \iiiint \langle S(\boldsymbol{y}) S(\boldsymbol{y}+\boldsymbol{r}) | \boldsymbol{n}, \boldsymbol{b}, S_0; \mathscr{D} \rangle_d \ |\boldsymbol{r}|^{-1} Q(S_0) \mathscr{P}_1(\boldsymbol{n}) \mathscr{P}_2(\boldsymbol{b}) \ \mathrm{d}\boldsymbol{r} \, \mathrm{d}\boldsymbol{n} \, \mathrm{d}\boldsymbol{b} \, \mathrm{d}S_0 \\
&\approx \frac{1}{4\pi} \iiiint S_0^2 \Theta(r_1/l_1, r_2/l_2, r_3/l_3) \ |\boldsymbol{r}|^{-1} Q(S_0) \mathscr{P}_1(\boldsymbol{n}) \mathscr{P}_2(\boldsymbol{b}) \ \mathrm{d}\boldsymbol{r} \, \mathrm{d}\boldsymbol{n} \, \mathrm{d}\boldsymbol{b} \, \mathrm{d}S_0 \\
&\approx \iiint S_0^2 l_2 l_3 \Theta_0(\delta_2, \delta_3) \ Q(S_0) \mathscr{P}_1(\boldsymbol{n}) \mathscr{P}_2(\boldsymbol{b}) \mathrm{d}\boldsymbol{n} \, \mathrm{d}\boldsymbol{b} \, \mathrm{d}S_0,
\end{aligned} \tag{4.34}$$

$$\Theta_0(\delta_2, \delta_3) = \frac{1}{4\pi} \int \frac{\Theta(\boldsymbol{a})}{\sqrt{a_1^2 + \delta_2^2 a_2^2 + \delta_3^2 a_2^2}} \, \mathrm{d}\boldsymbol{a}, \tag{4.35}$$

where $\delta_i(S_0) = l_i / l_1(S_0)$, and $Q(S_0), \mathscr{P}_1(\boldsymbol{n})$ and $\mathscr{P}_2(\boldsymbol{b})$ are the PDFs for $S_0, \boldsymbol{n}$ and $\boldsymbol{b}$, respectively.

Our definition of the coherent structure requires that $l_1 \gg l_2$ and $l_1 \gg l_3$. Recalling that the lengths $l_i(S_0)$ are independent of $\boldsymbol{n}$ and $\boldsymbol{b}$, and performing the ensemble average over the isotropic distribution $\mathscr{P}_1(\boldsymbol{n}) = \frac{1}{4}\pi$ and $\mathscr{P}_2(\boldsymbol{b}) = \frac{1}{2}\pi$, we obtain to leading order of δ_i

$$\begin{aligned}
\langle (\nabla p)^2 \rangle &\approx \int \ S_0^2 \Theta_0(S_0) l_2(S_0) l_3(S_0) \ Q(S_0) \, \mathrm{d}S_0 \\
&\approx \left(\frac{\bar{\epsilon}}{v} \right)^2 \int \chi^2 \Theta_0(\chi) \ l_2(\chi) l_3(\chi) \bar{Q}(\chi) \, \mathrm{d}\chi,
\end{aligned} \tag{4.36}$$

where $\bar{Q}$ is the normalized PDF for the normalized source term $\chi \equiv \bar{S}_0 / (\bar{\epsilon}/v)$. Since $\Theta_0(S_0) l_2(S_0) l_3(S_0)$ is a slowly varying function of S_0, and $\bar{Q}(\chi)$ falls rapidly for large amplitude when all moments of χ exist, the function $\chi^2 \bar{Q}(\chi)$ has a pronounced maximum at χ_* and the average over χ, (4.36), can be approximated as

$$\langle (\nabla p)^2 \rangle \approx \left(\frac{\bar{\epsilon}}{v} \right)^2 \ (l_{er}(\chi_*))^2 \ J(\chi_*), \tag{4.37}$$

$$(l_{er}(\chi_*))^2 \equiv l_2(\chi_*) l_3(\chi_*), \tag{4.38}$$

$$J(\chi_*) = \int \chi^2 \Theta_0(\chi) \left(\frac{l_2(\chi) l_3(\chi)}{l_2(\chi_*) l_3(\chi_*)} \right) \bar{Q}(\chi) \, \mathrm{d}\chi, \tag{4.39}$$

where $l_{er}(\chi_*)$ is an effective length formed by l_2 and l_3. Equation (4.37) shows that the variance of the pressure gradient is given by the product of the amplitude $\left(\bar{\epsilon}/v\right)^2$ and $l_2(\chi_*) l_3(\chi_*)$.

Step 3.

Since $l_i(\chi)$ are functions of $\chi = S_0/(\bar{\epsilon}/\nu)$, change of the level of S_0 implies variation of the average shape of the domain D_α, which corresponds to visualization of iso-surfaces of $S(\boldsymbol{x})$. Therefore we must determine $l_{er}^2(\chi_*)$, that is, the shape of $\bar{D}$. The problem is to determine the average shape of regions in which $S(\boldsymbol{x})$ is larger than a given threshold value. Our approach to this problem is empirical.

We must first determine the value of χ_*. The general form of the PDF $\bar{Q}(\chi)$ is known (for example, see figure 20 in Gotoh *et al.* 1993, figure 5 in Cao *et al.* 1999) but its precise analytical form is not. However, we can find a reasonable approximation of $\bar{Q}(\chi_*)$ as follows. Suppose that a typical component of the velocity gradient, normalized by $(\bar{\epsilon}/\nu)^{1/2}$, is represented as $\xi \approx u_{i,j}/(\bar{\epsilon}/\nu)^{1/2}$ and that the normalized source term is approximated as

$$\chi = \beta\xi^2 \tag{4.40}$$

in which β is a positive constant of order unity. Let $\overline{\Psi}(\xi)$ be the PDF for ξ, then the mapping (4.40) gives

$$\bar{Q}(\chi) = \overline{\Psi}(\xi)\left(\frac{\mathrm{d}\chi}{\mathrm{d}\xi}\right)^{-1}. \tag{4.41}$$

Kraichnan (1990) finds that the PDF for a single component of the velocity gradient is approximately

$$\Psi(\xi) \approx \left(\frac{1}{8\pi\langle\xi_0^2\rangle|\xi|}\right)^{1/2}\exp\left(-\frac{\bar{\epsilon}|\xi|}{2\nu\langle\xi_0^2\rangle}\right), \tag{4.42}$$

where $\langle\xi_0^2\rangle$ is the variance of one component of the velocity gradient in a Gaussian velocity field. Using $\bar{\epsilon} = 15\nu\langle(\partial u_1/\partial x_1)^2\rangle = 15\bar{\epsilon}\langle\xi^2\rangle$, and assuming $\langle\xi_0^2\rangle$ equal to $(\bar{\epsilon}/\nu)\langle\xi^2\rangle$, (4.42) becomes

$$\overline{\Psi}(\xi) \approx N|\xi|^{-1/2}\exp\left(-\frac{15|\xi|}{2}\right), \tag{4.43}$$

where N is a normalization constant. Substituting (4.43) into (4.41) we obtain

$$\bar{Q}(\chi) \approx \frac{N}{2\beta^{1/4}|\chi|^{3/4}}\exp\left(-\frac{15}{2}\left(\frac{|\chi|}{\beta}\right)^{1/2}\right). \tag{4.44}$$

This PDF for χ is consistent with the negative tail of the PDF in figure 20 of Gotoh *et al.* (1993). The value of χ_* can be found from $\mathrm{d}\left(\chi^2\bar{Q}(\chi)\right)/\mathrm{d}\chi = 0$ as $\chi_* = \beta/9$, $\xi_*^2 = \chi_*/\beta = \frac{1}{9}$. Since $\nu\langle\boldsymbol{\omega}^2\rangle = \bar{\epsilon} = 15\bar{\epsilon}\langle\xi^2\rangle$ in isotropic turbulence, we have an estimate for the threshold value of the vorticity as $\boldsymbol{\omega}_*^2/\langle\boldsymbol{\omega}^2\rangle = \boldsymbol{\omega}_*^2/(\bar{\epsilon}/\nu) = 15\xi_*^2 = 15/9 \approx 1.7$. Recent computer visualization of the vorticity and strain fields has shown that domains with magnitudes higher than a given threshold value of $\boldsymbol{\omega}_*^2/\langle\boldsymbol{\omega}^2\rangle \approx (u_{i,j})_*^2/\langle u_{i,j}^2\rangle$ are a blob, sheet, or tube (She *et al.* 1991; Cao *et al.* 1999; Tsinober 1998). The threshold value $(u_{i,j})_*^2/\langle u_{i,j}^2\rangle \approx 1.7$ seems to correspond to sheets or ribbons in the visualizations with lengths $L \sim l_1 \gg l_2(l_3)$ (Tsinober 1998).

Substitution of χ_* into $l_i(\chi_*)$ leads to an estimate of the width and thickness of the sheet with threshold $S_{0*} = \chi_*(\bar{\epsilon}/\nu)$. The axial lengths of the strongest vortical structures observed in the simulations are of the order of the integral scale, so we expect l_1 also to be of that order, but there are several candidates for the cross-sectional lengths l_2, l_3. These include the Taylor microscale λ and the Kolmogorov scale η. Among the various combinations for $l_{er}^2(\chi_*) = l_2(\chi_*)l_3(\chi_*)$, the choice, $l_2(\chi_*) = \lambda, l_3(\chi_*) = \eta$

gives the observed $\mathscr{R}_\lambda^{1/2}$ dependence. The first author has recently examined in detail the structure of S within a series of forced DNS in the range $\mathscr{R}_\lambda = 28 \sim 68$, and found that the average volume of $\bar{D}$ for the dominant threshold value $S_{0*}/(\bar{\epsilon}/\nu) \sim 2$ is approximately $L \times \lambda \times \eta$ independent of $\mathscr{R}_\lambda$. This implies $l_{er}^2(\chi_*) = \lambda \times \eta$. However, as stated in the previous section, at high Reynolds number we expect Kolmogorov scaling and $l_{er}^2(\chi_*) \propto \eta^2$. The variance of the pressure gradient is from (4.37)

$$\left\langle (\nabla p)^2 \right\rangle \approx C_{\nabla p} \left(\frac{\bar{\epsilon}}{\nu} \right)^2 \lambda\eta \propto \frac{\bar{\epsilon}^{3/2}}{\nu^{1/2}} \mathscr{R}_\lambda^{1/2}, \tag{4.45}$$

where we have used $\lambda \sim \mathscr{R}_\lambda^{1/2}\eta$, and $C_{\nabla p}$ is a quantity of order unity:

$$C_{\nabla p} = J(\chi_* = \beta/9). \tag{4.46}$$

More precisely, $C_{\nabla p}$ depends very weakly on $\mathscr{R}_\lambda$, at most $O(\ln \mathscr{R}_\lambda)$ when the domain $\bar{D}$ is a long tube, and can be regarded as constant when compared to $\mathscr{R}_\lambda{}^{1/2}$.

In a recent paper Jiménez & Wray (1997) investigated the smallest features within the same simulations used in this study. These are strong vortex tubes, having lengths of the order of the integral scale, diameters of the order of the Kolmogorov scale, and azimuthal velocities of the order of the mean turbulent intensity. The pressure gradient within the vortices, in Kolmogorov units, is then of order $\mathscr{R}_\lambda$. The volume fraction occupied by the vortices was found to be of order $\mathscr{R}_\lambda^{-2}$, so that their contribution to the normalized pressure-gradient variance $F_{\nabla p}$ is of order unity. As we have demonstrated above, the dominant order $\mathscr{R}_\lambda^{1/2}$ contributions to $F_{\nabla p}$ are made by structures with diameters of order $(\lambda\eta)^{1/2}$ which probably surround the strong vortex tubes. The convergence of the integral (4.16) requires that the positive and negative source terms be equally probable. Therefore we cannot include the strong vorticity alone in the computation of $F_{\nabla p}$ and this argument supports the fact that the domain $\bar{D}$ cannot be a long vortex tube with the volume $L \times \eta \times \eta$.

When the effect of intermittency of the amplitude of S^2 is taken into account, we must replace $\bar{\epsilon}$ by its volume-averaged dissipation rate $\epsilon_{r_{er}}$ with $r_{er} = (L_1\lambda\eta)^{1/3}$, where $L_1\lambda\eta$ is the average volume of the sheet having threshold $\chi_* = \beta/9$. Using $L_1 \sim \mathscr{R}_\lambda^{3/2}\eta$ and the refined Kolmogorov theory (or another model such as the Log Poisson model of She & Lévêque (1994), with the same second-order moments of ϵ_r), we have $\left\langle \epsilon_{r_{er}}^2 \right\rangle \propto \bar{\epsilon}^2 (L_1/r_{er})^\mu$. Replacing $\bar{\epsilon}$ in (4.45) by $\left\langle \epsilon_{r_{er}}^2 \right\rangle^{1/2} \propto \bar{\epsilon}(L_1/r_{er})^{\mu/2} \propto (\mathscr{R}_\lambda^{5/6})^{\mu/2}$, we obtain

$$\left\langle (\nabla p)^2 \right\rangle \approx C'_{\nabla p} \frac{\bar{\epsilon}^{3/2}}{\nu^{1/2}} \mathscr{R}_\lambda^{1/2+5\mu/8} \propto \frac{\bar{\epsilon}^{3/2}}{\nu^{1/2}} \mathscr{R}_\lambda^{0.625}, \tag{4.47}$$

where $C'_{\nabla p}$ is a constant of order unity. The slope of $F_{\nabla p}$ in figure 1, determined by the least-square fit, is found to be 0.64, which is very close to the value of (4.47). This small correction to the exponent would appear in the analysis above as a weak variation of the PDF $Q(S_0)$ with $\mathscr{R}_\lambda$ and a corresponding small change in $C'_{\nabla p} = J'(\chi_*)$.

The spatial coherency of the source term S is crucial in our discussion since the space integral is taken only over domains having values larger than a given threshold. If the spatial coherency of S is broken by cutting those domains into many pieces with a single length scale of order η, and distributing them uniformly in space, then the variance of the pressure gradient becomes independent of $\mathscr{R}_\lambda$ by (4.37) while the PDF for S is unchanged.

This is essentially what occurs in the case of the Gaussian velocity field having the same energy spectrum as that of turbulence. The spectrum of $\epsilon_G(\boldsymbol{x})$ has a support

centred on $k\eta \approx 0.3$ (see figure 8) and this means that $\tilde{l}_1 = \tilde{l}_2 = \tilde{l}_3 \approx \eta$ is the only available characteristic length. The variance of the pressure gradient becomes by (4.37)

$$\langle (\nabla p)^2 \rangle_G \approx C^G_{\nabla p} \left(\frac{\bar{\epsilon}}{\nu} \right)^2 \eta^2 = C^G_{\nabla p} \frac{\bar{\epsilon}^{3/2}}{\nu^{1/2}}, \tag{4.48}$$

so that the normalized variance is independent of $\mathscr{R}_\lambda$. Here $C^G_{\nabla p}$ is a constant of order unity and independent of $\mathscr{R}_\lambda$.

The discussion above suggests that there are aspects of pressure intermittency that are not described by the PDF alone, and that the pressure-gradient variance is a typical example in which the spatial configuration of domains having large amplitudes within small volumes is an essential ingredient.

5. Summary and discussion

Pressure statistics have been examined within a DNS of stationary (forced) isotropic turbulence. The energy spectra at the computed Reynolds numbers collapse under Kolmogorov scaling, but the pressure spectra do not. It is found that the Gaussian approximation to the fourth-order moments of the velocity derivatives underestimates the variances of the pressure and pressure gradient of the DNS fields. The pressure variance is insensitive to the microscale Reynolds number. On the other hand, small-scale statistics of the pressure such as the normalized pressure-gradient variance and the pressure spectrum at high wavenumber show a strong Reynolds number dependence of roughly $\mathscr{R}_\lambda^{1/2}$. A $k^{-5/3}$ range is observed in the pressure spectra and its span increases with Reynolds number. The Gaussian approximation applied to the observed $k^{-5/3}$ range in the energy spectrum gives a $k^{-7/3}$ range in the pressure spectrum. Despite the uncertainty about the length of the $k^{-5/3}$ range at high Reynolds number it seems clear that the coexistence of $k^{-7/3}$ and $k^{-5/3}$ ranges in the pressure spectrum is plausible in forced turbulence.

A weak growth of intermittency across the pressure spectrum, characterized by the ratio of power spectra $P(k)/P_G(k)$, was found to be proportional to $(2\mu/9)\mathscr{R}_\lambda^{1/2} \log(k\eta)$ for $k\eta < \frac{1}{2}$.

The intermittency effects of the small-scale velocity field also appear in the one-point PDFs for the pressure and pressure gradient. The one-point PDF of the pressure has a nearly exponential tail for negative fluctuations while that of the pressure gradient is symmetric and of stretched exponential form with exponents decreasing from unity with $\mathscr{R}_\lambda$.

To understand the physics of the $\mathscr{R}_\lambda^{1/2}$ dependence required to scale the small-scale statistics of the pressure field, we found the pressure-gradient variance within a model field that is consistent with several known exact constraints. The model field consists of an infinite set of coherent domains D_α in each of which the source term of the Poisson equation for pressure takes positive and negative values above a given threshold magnitude. It should be stressed that the configuration of high-vorticity domains accompanied by high-strain domains is required for the convergence of the integral (4.16). The pressure field in this model is analogous to the electro-static potential produced by randomly distributed charge dipoles. In our case the randomly distributed objects are the coherent structures consisting of a pair of high-vorticity and -strain domains. The pressure-gradient variance takes the form of a product of the square of the representative amplitude of the source term, averaged over the

domains D_α, and an effective volume of the averaged domain $\bar{D}$ divided by the integral scale,

$$\langle (\nabla p)^2 \rangle \approx \frac{\langle S^2 | \mathscr{D} \rangle \times (\text{effective volume})}{(\text{integral scale})}$$

$$\approx \langle S^2 | \mathscr{D} \rangle \times (\text{effective cross-sectional area}). \tag{5.1}$$

An $\mathscr{R}_\lambda^{1/2}$ dependence follows from the choice of the Taylor microscale λ and Kolmogorov scale η as the shorter two characteristic lengths of the coherent structures in the model. The notion of the effective volume of a domain, averaged over many coherent domains D_α, is an essential feature of the model. Even when the amplitude S has the same average value as given by the Gaussian approximation, it is the existence of the coherent structure that mostly determines the Reynolds number power-law dependence. The effect of the intermittency of S amplitudes, which Yeung & Pope (1989) and Hill & Wilczak (1995) considered, gives only a small correction to the exponent.

The above picture is totally dependent on the accuracy of the model, and this can be tested by checking model consistency with known exact constraints and other observed results. As an example, consider the dissipation spectrum obtained from the model. Recall that $S(\boldsymbol{x}) = \boldsymbol{\omega}^2(\boldsymbol{x})/2 - \sigma^2(\boldsymbol{x}) \sim \epsilon(\boldsymbol{x})/\nu$, from which we expect coherent structure of the dissipation $\epsilon(\boldsymbol{x})$ as well as $S(\boldsymbol{x})$. Since the model contains one macroscale length L, and two small scale lengths λ and η the spectrum $E_\epsilon^{model}(k)$ computed from the model field has excitation at low wavenumbers as well as at wavenumbers near $1/\lambda$ and $1/\eta$, which is consistent with $E_\epsilon(k)$ of figure 8.

It should be stressed that the $\mathscr{R}_\lambda{}^{1/2}$ dependence of $F_{\nabla p}$ discussed in this paper is found within forced DNS at low to moderate Reynolds numbers. The same behaviour was reported in Vedula & Yeung (1999) where the forcing mechanism differed in detail from the present DNS but retained its basic property of a small sample of energetic and highly correlated Fourier modes at the largest scale available. Although we expect that decaying turbulence as studied by Batchelor (1951) exhibits universal equilibrium statistics at lower Reynolds number than such forced flows do, the forced results suggest that equilibrium for pressure statistics requires a higher Reynolds number than equilibrium for velocity statistics, a situation that is not compatible with the Gaussian approximation. Recent experimental measurements by Voth *et al.* (1998) in stationary turbulence between counter-rotating disks strongly suggest that $F_{\nabla p}$ is independent of $\mathscr{R}_\lambda$ at $\mathscr{R}_\lambda = 1000$–$2000$ but is greater than the value predicted by the Gaussian approximation (M. Nelkin 1998, personal communication; Voth *et al.* 1998). Although the forcing mechanism is different from that used in the DNS (where there is no mean flow), the behaviour at low Reynolds number would quite likely be similar and a composite form such as (3.14) provides a possible interpolation between the DNS and experimental results. Within the model $F_{\nabla p}$ becomes independent of $\mathscr{R}_\lambda$ when the characteristic lengths of the small-scale vortical structures (and their surrounding strain fields) are some multiple of the Kolmogorov scale (possibly large multiples) and the disparity of the scales becomes limited by instability.

The authors thank Dr Alan Wray for extending his decaying simulation to lower Reynolds numbers and for measuring the pressure-gradient variance within the archived fields and Professor J. Jiménez for providing the preprint of Jiménez & Wray (1997). The authors have benefited from fruitful discussions with Professors E.

Bodenschatz, Y. Kaneda, M. Nelkin, D. Pullin, Z. She, P. K. Yeung and Drs R. H. Kraichnan, S.-Y. Chen and Y. Zhou. T. G. expresses his deep thanks to Professor Moin for his hospitality at the CTR and to the Tatemastu foundation for partial support. The computations were done at NASA Ames Research Centre during the 1994 Summer Program of the Center for Turbulence Research.

REFERENCES

Batchelor, G. K. 1951 Pressure fluctuations in isotropic turbulence. *Proc. Camb. Phil. Soc.* **47**, 359–374.

Batchelor, G. K. 1953 *The Theory of Homogenous Turbulence*. Cambridge University Press.

Cadot, O., Douady, S. & Couder Y. 1995 Characterization of the low-pressure filaments in a three-dimensional turbulent shear flow. *Phys. Fluids* **7**, 630–646.

Cao, N., Chen, S. & Doolen, G. D. 1999 Statistics and structures of pressure in isotropic turbulence. *Phys. Fluids* **11**, 2235–2250.

Chandrasekhar, S. 1949 On Heisenberg's elementary theory of turbulence. *Proc. R. Soc. Lond.* A **200**, 20–33.

Chen, H., Herring, J. R., Kerr, R. M. & Kraichnan, R. H. 1989 Non-Gaussian statistics in isotropic turbulence. *Phys. Fluids* A **1**, 1844–1854.

Collis, D. C. 1948 The diffusion process in turbulent flow. *Div. of Aeronautics, Counc. Sci. Industr. Res. Australia, Rep.* A 55.

Comte-Bellot, G. & Corrsin, S. 1971 Simple Eulerian time correlation of full and narrow band velocity signals in grid-generated, 'isotropic' turbulence. *J. Fluid Mech.* **48**, 273–337.

George, W. K., Beuther, P. D. & Arndt, R. E. A. 1984 Pressure spectra in turbulent free shear flows. *J. Fluid Mech.* **148**, 155–191.

Gotoh, T. & Rogallo, R. S. 1994 Statistics of pressure and pressure gradient in homogeneous isotropic turbulence. *Proc. 1994 Summer Program*, pp. 189–205. Center for Turbulence Research, Stanford.

Gotoh, T., Rogallo, R. S., Herring, J. R. & Kraichnan, R. H. 1993 Lagrangian velocity correlations in homogeneous isotropic turbulence. *Phys. Fluids* A **5**, 2846–2864.

Heisenberg, W. 1948 Zur statistischen Theorie der Turbulenz. *Z. Physik* **124** 628–657.

Hill, R. J. 1996 Pressure-velocity-velocity statistics in isotropic turbulence. *Phys. Fluids* **8**, 3085–3093.

Hill, R. J. & Boratav, O. N. 1997 Pressure statistics for locally isotropic turbulence. *Phys. Rev.* E **56**, R2363–2366.

Hill, R. J. & Thoroddsen, S. T. 1997 Experimental evaluation of acceleration correlations for locally isotropic turbulence. *Phys. Rev.* E **55**, 1600–1606.

Hill, R. J. & Wilczak, J. M. 1995 Pressure structure functions and spectra for locally isotropic turbulence. *J. Fluid Mech.* **296**, 247–269.

Holzer, M. & Siggia, E. 1993 Skewed, exponential pressure distributions from Gaussian velocities. *Phys. Fluids* A **5**, 2525–2532.

Jiménez, J. & Wray, A. A. 1997 On the characteristics of vortex filaments in isotropic turbulence. *J. Fluid Mech.* **373**, 255–285.

Jiménez, J., Wray, A. A., Saffman, P. G. & Rogallo, R. S. 1993 The structure of intense vorticity in isotropic turbulence. *J. Fluid Mech.* **255**, 65–90.

Kerr, R. M. 1985 High-order derivative correlations and the alignment of small-scale structures in isotropic numerical turbulence. *J. Fluid Mech.* **153**, 31–58.

Kolmogorov, A. N. 1962 A refinement of previous hypotheses concerning the local structure of turbulence in a viscous incompressible fluid at high Reynolds number. *J. Fluid Mech.* **13**, 82–85.

Kraichnan, R. H. 1956 Pressure field within homogeneous anisotropic turbulence. *J. Acoustic Soc. Am.* **28**, 64–72.

Kraichnan, R. H. 1990 Models of intermittency in hydrodynamic turbulence. *Phys. Rev. Lett.* **65**, 575–578.

Liepmann, H. W., Laufer, J. & Liepmann, K. 1951 On the spectrum of isotropic turbulence. *NACA Tech. Note* 2473.

MAXEY, M. R. 1987 The gravitational settling of aerosol particles in homogeneous turbulence and random fields. *J. Fluid Mech.* **174**, 441–465.

MÉTAIS, O. & LESIEUR, M. 1992 Spectral large-eddy simulation of isotropic and stably stratified turbulence. *J. Fluid Mech.* **239**, 157–194.

MONIN, A. S. & YAGLOM, A. M. 1975 *Statistical Fluid Mechanics*, Vol. 2. MIT press.

NELKIN, M. 1994 Universality and scaling in fully developed turbulence. *Adv. Phys.* **43**, 143–181.

PRASKOVSKY, A. & ONCLEY, S. 1994 Measurements of the Kolmogorov constant and intermittency exponent at very high Reynolds numbers. *Phys. Fluids* A **6**, 2886–2888.

PULLIN, D. I. & ROGALLO, R. S. 1994 Pressure and higher-order spectra for homogeneous isotropic turbulence. *Proc. 1994 Summer Program*, pp. 177–187. Center for Turbulence Research, Stanford.

PUMIR, A. 1994 A numerical study of pressure fluctuations in three-dimensional, incompressible, homogeneous, isotropic turbulence. *Phys. Fluids* **6**, 2071–2083.

SCHUMANN, U. & PATTERSON, G. S. 1978 Numerical study of pressure and velocity fluctuations in nearly isotropic turbulence. *J. Fluid Mech.* **88**, 685–709.

SHE, Z. S., JACKSON, E. & ORSZAG, S. A. 1991 Structure and dynamics of homogeneous trubulence: models and simulations. *Proc. R. Soc. Lond.* A **434**, 101–124.

SHE, Z. S. & LÉVÊQUE, E. 1994 Universal scaling laws in fully developed turbulence. *Phys. Rev. Lett.* **72**, 336–339.

SREENIVASAN, K. R. & KAILASNATH, P. 1993 An update on the intermittency exponent in turbulence. *Phys. Fluids* A **5**, 512–514.

TENNEKES, H. & LUMLEY, J. L. 1972 *A First Course in Turbulence*. The MIT press.

TSINOBER, A. 1998 Turbulence: beyond phenomenology. In *Chaos, Kinetics and Nonlinear Dynamics in Fluids and Plasmas* (ed. S. Benkadda & G. M. Zaslavsky). Springer.

UBEROI, M. S. 1953 Quadruple velocity correlations and pressure fluctuations in isotropic turbulence. *J. Aero. Sci.* **20**, 197–204.

UBEROI, M. 1954 Correlations involving pressure fluctuations in homogeneous turbulence. *NACA Tech. Note* 3116.

UBEROI, M. S. & CORRSIN, S. 1952 Diffusion of heat from a line source in isotropic turbulence. *NACA Tech. Note* 2710.

VAN ATTA, C. W. & WYNGAARD, J. C. 1975 On higher-order spectra of turbulence. *J. Fluid Mech.* **72**, 673–694.

VEDULA, P. & YEUNG, P. K. 1999 Similarity scaling of acceleration and pressure statistics in numerical simulations of isotropic turbulence. *Phys. Fluids* **11**, 1208–1220.

VOTH, G. A., SATYANARAYAN & BODENSCHATZ, E. 1998 Lagrangian acceleration measurements at large Reynolds numbers. *Phys. Fluids* **10**, 2268–2280.

WRAY, A. A. 1997 A numerical simulation of decaying isotropic turbulence. In *A database for the validation of LES computations in transition and turbulence* (ed. J. Jiménez). *AGARD R-345, data set HOM02.*

YEUNG, P. K. 1996 Lagrangian and Eulerian statistics of fluid acceleration in isotropic turbulence. *Bull. Am. Phys. Soc.* **41**, 1727.

YEUNG, P. K. & POPE, S. B. 1989 Lagrangian statistics from direct numerical simulations of isotropic turbulence. *J. Fluid Mech.* **207**, 531–586.